Lawrence Berkeley Laboratory
UNIVERSITY OF CALIFORNIA

Physics Division

MEASUREMENT OF THE INCLUSIVE BRANCHING FRACTION $\tau^- \rightarrow \nu_\tau \pi^- \pi^0$ + NEUTRAL MESON(S)

W.W. Moses
(Ph.D. Thesis)

December 1986

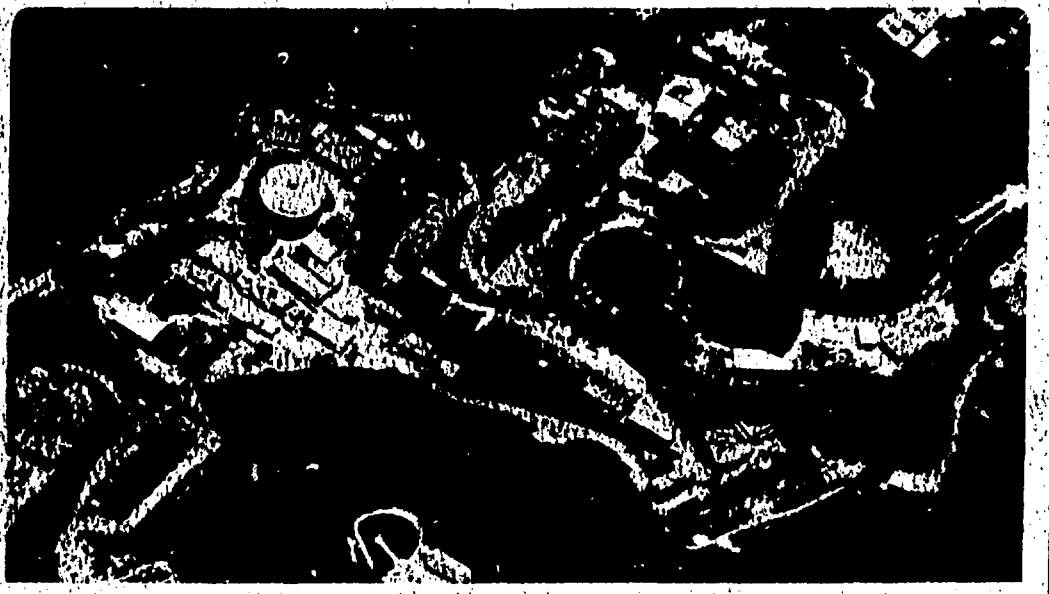

Prepared for the U.S. Department of Energy under Contract DE-AC03-76SF00098

LBL-22579
TPC-LBL-86-20

Measurement of the Inclusive Branching Fraction $\tau^- \rightarrow \nu_\tau \pi^- \pi^0 +$ neutral meson(s)

LBL--22579

DE87 004592

By
William Walton Moses
Ph.D. Thesis
December 1, 1986

Lawrence Berkeley Laboratory
University of California
Berkeley, CA 94720

Abstract

This dissertation measures an inclusive branching fraction of $(13.9 \pm 2.0^{+2.1}_{-2.4})\%$ for the decay $\tau^- \rightarrow \nu_\tau \pi^- \pi^0 + n h^0$, where h^0 is a π^0 or an η and $n \geq 1$. The data sample, obtained with the TPC detector facility at PEP, corresponds to an integrated luminosity of 72 pb^{-1} at 29 GeV center of mass energy. The measured value for this branching fraction is somewhat greater than the theoretical prediction and, taking errors into account, resolves the present difference between the inclusive and the sum of the exclusive τ^- branching fractions into one charged prong. In addition, a lower limit of 8.3% (95% CL) is placed on the branching fraction $B(\tau^- \rightarrow \nu_\tau \pi^- \pi^0 \pi^0)$.

This work is supported by the United States Department of Energy under Contract DE-AC03-76SF00098.

Contents

Acknowledgements

It is impossible to thank everybody who has helped me through my career as a graduate student, therefore I apologize to all those who are not explicitly mentioned here, and hasten to add that your efforts are appreciated. I would like to thank my advisors, Roy Kerth and Bill Wenzel, for giving me both direction and the freedom to choose the projects that I worked on. I thank Hiro Aihara and Masa Yamauchi, who worked side by side with me during much of the development of the Hex. I have learned a tremendous variety of practical skills from the technicians, machinists, and engineers at LBL, especially Fred Goozen and Tom Webber, who taught me how a detector is really made. I owe a lot to the people who made the TPC work, especially Al Clark, Margie Shapiro, Peter Robrish, Al Bross, Dick Kofler, Dick Adachi, and Ed Lampo. I enjoyed the camaraderie among the people that worked on the trigger, namely Mitch Wayne, Mike Ronan, Bill Gary, and Kevin Derby, and am still amazed at the amount of work that we accomplished in six months. Finally, I would like to thank Steve Kaye, Werner Hofmann, Hiro Yamamoto, and Gerry Lynch, who taught me how to do a physics analysis, and Ed Whipple, who taught me how to distinguish good things from bad things, especially with respect to computers.

It would have been impossible for me to complete this project without the friendships that I developed along the way. The TPC had as nice a group of collaborators as anybody could ask for and the graduate students at LBL were particularly fun to work with. I am especially indebted to the SDRC (you know who you are) who made me feel human at least once each week. I thank Steve Sharpe, with whom I discovered rock climbing as a cure for frustration, and owe a huge debt of gratitude to DH & Susan, MJ & Tim, and Bruce & Kim for their companionship, sofa-beds, and flaming chocolate waffles. Finally, stealing a line from Peter Meyers, I thank my parents, Alan and Joanne Moses, who must have wondered what I have been doing all this time, and Martha Davies, who knows.

Chapter 1

Introduction

Over the past several years there has been increasing interest in measuring the exclusive decay modes of the tau lepton. This interest is sparked by the fact that the measurement of the inclusive single prong branching fraction is significantly larger than the sum of the exclusive one prong decay fractions [1]. Such disagreements are typically due to decay modes that have not yet been observed or to systematic errors associated with the existing measurements, but most of the predicted decay modes of the τ^- have been observed and the errors on their measured branching fractions are significantly smaller than the discrepancy. There are a few expected decay modes that have not yet been measured, but strong theoretical predictions exist for their branching fractions, and these are too small to account for the discrepancy.

The measured inclusive branching fractions of the τ^- into one, three, and five charged particles are $B_1 = (86.5 \pm 0.3)\%$, $B_3 = (13.4 \pm 0.3)\%$, and $B_5 = (0.15 \pm 0.04)\%$ [2,3,4]. The well-measured exclusive single prong branching fractions are listed in Table 1.1 [5]. They sum to $(68.9 \pm 2.0)\%$, so the difference between the inclusive and the sum of the exclusive fractions is $(17.6 \pm 2.0)\%$.

One explanation for the difference between inclusive and measured exclusive branching fractions is that the branching fractions for decay modes that in-

Decay Mode	Measured Branching Fraction (%)
$\tau^- \to e^- \overline{\nu}_e \nu_\tau$	17.4 ± 0.5
$\tau^- \to \mu^- \overline{\nu}_\mu \nu_\tau$	17.6 ± 0.6
$\tau^- \to \pi^- \nu_\tau$	10.1 ± 1.1
$\tau^- \to \rho^- \nu_\tau$	22.1 ± 1.4
$\tau^- \to K^- \nu_\tau (+neutrals)$	1.7 ± 0.4
Sum	68.9 ± 2.0

Table 1.1: Measured Single Prong Branching Fractions of the τ^-

Decay Mode	Predicted Branching Fraction (%)
$\tau^- \rightarrow \pi^-\pi^0\pi^0\nu_\tau$	7.1
$\tau^- \rightarrow \pi^-\pi^0\pi^0\pi^0\nu_\tau$	1.0
$\tau^- \rightarrow \pi^-\pi^0\eta\nu_\tau$	0.5
$\tau^- \rightarrow \pi^-\eta\eta\nu_\tau$	< 0.8

Table 1.2: Predicted One Prong Branching Fractions of the τ^-

volve more than one neutral meson contribute to B_1 but are not included in the sum of the exclusive branching fractions. Two such modes have been measured, $B(\tau^- \rightarrow \nu_\tau\pi^-\pi^0\pi^0) = (6.0 \pm 3.5)\%$ and $B(\tau^- \rightarrow \nu_\tau\pi^-\pi^0\pi^0\pi^0) = (3.0 \pm 2.7)\%$, but these have not been included in Table 1.1 due to their large errors [6]. Strong theoretical predictions exist for the multiple neutral meson branching fractions [1], and their expected contributions to B_1 are listed in Table 1.2. However, the sum of these predicted branching fractions is only 9.4%, significantly smaller than the $(17.6 \pm 2.0)\%$ difference between the inclusive and sum of the exclusive branching fractions.

It is apparent that a significant discrepancy exists. When the measured exclusive one prong branching fractions are summed and the theoretical predictions for the branching fractions that have not yet been measured are added to this sum, the total is substantially less than the measured inclusive one prong branching fraction. This dissertation attempts to resolve this discrepancy by measuring the inclusive branching fraction $B(\tau^- \rightarrow \nu_\tau\pi^-\pi^0 + \mathrm{n}h^0)$, where $\mathrm{n} \geq 1$ and h^0 is a π^0 or an η. The measurement of this inclusive branching fraction may also determine why the theoretical prediction for this discrepancy is incorrect. If the measured value of this branching fraction agrees with the theoretical prediction (i.e. 9.4%), then there must be an unexpected decay mode (or modes) that accounts for the rest of the difference. If the measured value of the multiple neutral meson branching fraction is equal to the entire difference (i.e. 17.6%), then the theoretical prediction for one (or more) of the individual multiple neutral meson branching fractions is incorrect.

This dissertation begins with a discussion of the theoretical predictions for the τ^- branching fractions, with special attention paid to the predictions for the single prong decay modes. This is followed by descriptions of the TPC detector system, which is used to measure the τ^- branching fractions, and the photon reconstruction algorithm, as the branching fraction measurements depend heavily on photon reconstruction. After a description of the $\tau^+\tau^-$ event selection, the first physics analysis is presented – the measurement of the branching fraction $\mathcal{B}(\tau^- \rightarrow \nu_\tau\rho^-)$. Finally, the multiple neutral meson branching fraction is measured and the results of the measurement discussed.

Chapter 2

Theory

The theoretical aspects of τ^- leptons are discussed in this chapter. The discussion begins by describing the measurements of the fundamental properties of the τ^-, especially those measurements that prove that the τ^- is a lepton. This is followed by theoretical predictions for the branching fractions of the τ^-, with special attention paid to the decay modes that involve a single charged particle, and a short discussion about the validity of the predictions. For the sake of simplicity, all reactions involving taus are expressed as τ^- reactions – the expressions are equally valid for the charge conjugate reactions.

2.1 The Standard Model

One of the greatest advances in high energy physics was the unification of the electromagnetic and weak nuclear forces by Glashow [7], Weinberg [8], and Salam [9]. This theory has become so widely accepted that it is commonly known as the standard model for the electro-weak interaction or just the standard model. In addition to treating the weak nuclear and electromagnetic forces, previously thought to be separate fundamental forces of nature, as two manifestations of the same force, the theory provides a relatively simple framework for classifying subatomic particles. The fundamental particles are characterized either as gauge bosons (γ, $W^{\pm}$, and Z^0), the Higgs, or point-like fermions. The quark fermions are combined into three isospin doublets

$$\begin{pmatrix} u \\ d' \end{pmatrix} \begin{pmatrix} c \\ s' \end{pmatrix} \begin{pmatrix} t \\ b' \end{pmatrix},$$

as are the leptons

$$\begin{pmatrix} \nu_e \\ e^- \end{pmatrix} \begin{pmatrix} \nu_\mu \\ \mu^- \end{pmatrix} \begin{pmatrix} \nu_\tau \\ \tau^- \end{pmatrix}.$$

The mass and lifetime of each lepton is listed in Table 2.1 [5, pp.11-12].

Particle Type	Mass (MeV/c^2)	Lifetime (sec)
e^-	0.511	stable
ν_e	$< 4.6 \times 10^{-5}$	stable
μ^-	105.7	2.2×10^{-5}
ν_μ	< 0.25	stable
τ^-	1784	2.8×10^{-13}
ν_τ	< 70	stable

Table 2.1: Properties of the Leptons

2.1.1 The Tau Lepton

The τ^- particle was discovered by observing $e^+e^- \rightarrow e^\pm\mu^\mp$(+missing energy) interactions [10]. These anomalous events are explained as $e^+e^- \rightarrow \tau^+\tau^-$ events, where one $\tau^\pm$ decays into an $e^\pm$ and neutrinos and the other $\tau^\pm$ decays into a $\mu^\pm$ and neutrinos. By observing the rate at which these anomalous events occur as a function of the e^+e^- beam energy, the mass of the τ^- is determined to be (1784.2 ± 3.2) MeV/c^2 [11]. The observation of these $e^+e^- \rightarrow e^\pm\mu^\mp$ events is sufficient to prove the existence of the τ^- particle, but is not sufficient to prove that the τ^- is a lepton in the standard model. As all theoretical predictions for the properties of the τ^- particle assume that the τ^- is a lepton, the rest of this section is devoted to demonstrating that the τ^- is a lepton.

Leptons in the standard model of the electro-weak interaction are particles that interact only through the electro-weak interaction, have spin $\frac{1}{2}$, and no internal structure (ie. they are point-like particles). In addition, each charged lepton is associated with a neutrino and a lepton number conservation law.

All current measurements support the classification of the τ^- as a lepton in the standard electro-weak theory [12]. By studying the shape of the $e^+e^- \rightarrow \tau^+\tau^-$ cross section near the $\tau^+\tau^-$ production threshold, the spin of the τ^- is found to be consistent with the spin $\frac{1}{2}$ hypothesis and inconsistent with all other spin hypotheses for point-like particles [13]. Further measurement of the shape of the $e^+e^- \rightarrow \tau^+\tau^-$ cross section at higher energies shows that the τ^- is not a composite particle [14].

Several of the decay modes of the τ^- listed in Table 2.2 [5, p.12] are used to determine the forces that act on the τ^-. The decay modes $\tau^- \rightarrow e^-\overline{\nu}_e\nu_\tau$ and $\tau^- \rightarrow \mu^-\overline{\nu}_\mu\nu_\tau$ indicate that the τ^- interacts via the weak interaction, as these decay modes contain only leptons in their final state. In addition, the momentum spectrum of the e^- or μ^- from τ^- decay determines that these decays proceed via a V-A current, which is a signature of the weak interaction [15].

The presence of an associated neutrino is inferred by studying the momentum spectrum of the ρ^- in the decay $\tau^- \rightarrow \rho^-\nu_\tau$, which shows the flat distribution expected from a two body decay [12]. The neutrino associated with the τ^- is not a ν_e or a ν_μ, as this would allow decays of the type $\tau^- \rightarrow e^-\gamma$ and $\tau^- \rightarrow \mu^-\gamma$,

τ^- Decay Mode	Branching Fraction(%)
$e^-\overline{\nu}_e\nu_\tau$	17.4 ± 0.5
$\mu^-\overline{\nu}_\mu\nu_\tau$	17.6 ± 0.6
$\rho^-\nu_\tau$	22.1 ± 1.4
$\pi^-\nu_\tau$	10.1 ± 1.1
$K^{*-}\nu_\tau$	1.7 ± 0.7
$\pi^-\pi^+\pi^-\nu_\tau(+neutrals)$	13.4 ± 0.3

Table 2.2: Common τ^- Branching Fractions

which have not been observed [16]. The presence of a lepton conservation number associated with the τ^- is inferred from the momentum spectrum of the e^- or μ^- from τ^- decay. This momentum spectrum peaks a low momentum, which is consistent with a three body decay mode, but is inconsistent with a two body τ^- decay mode [15]. Since two body decays such as $\tau^- \rightarrow e^-\overline{\nu}_e$ or $\tau^- \rightarrow \mu^-\overline{\nu}_\mu$ would be allowed if there were no conserved lepton number associated with the τ^-, the presence of the ν_τ implies that there is a conserved lepton number associated with the τ^-.

It is difficult to prove that the τ^- does not interact via the strong interaction, as the only conclusive way to do this is to measure the τ^--hadron cross section, but τ^-'s decay far too quickly to both identify and collide them. However, the τ^- shows no evidence for decaying via the strong interaction, nor are its properties consistent with the properties of conventional hadrons. The τ^- is not a quark, as there is no evidence for a τ-$\overline{\tau}$ bound state slightly below $2m_\tau$ [5, p.83]. If the τ^- were a hadron, it would not be classified as a meson or a glueball as it has spin $\frac{1}{2}$, and so would be classified as a baryon. The long lifetime [17] and lack of hadronic decay modes such as $\tau^+ \rightarrow p^+\pi^0$ and $\tau^+ \rightarrow p^+K^0$ [5] suggest that if the τ^- were a baryon, it must possess a quantum number such as charm or bottom that forbids hadronic decays. However, the τ^- has a mass that is less than the mass of any of the charmed or bottom mesons and shows no sign of being a composite particle [14], which suggest that the τ^- is not a baryon.

The τ^- particle satisfies all of the requirements necessary to be a lepton. It interacts only through the electro-weak force, it has the proper spin characteristics, and has an associated neutrino and lepton number conservation law. Therefore, the τ^- is classified as a lepton in the standard model.

2.2 Lepton Decays in the Standard Model

In the standard model of the electro-weak interaction, leptons decay through a virtual W^- into a neutrino and a fermion-antifermion pair, as shown in Figure 2.1. In these decays, the fermion-antifermion pair (f_1 $\overline{f}_2$) must be partners in the same isospin doublet. If the isospin doublet is a lepton doublet, the

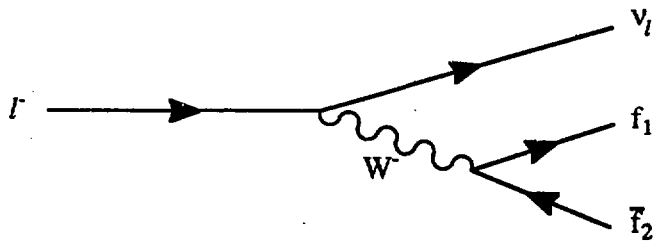

Figure 2.1: Lepton Decay Diagram

electro-weak theory can be used to calculate the partial decay width without approximations. However, if the isospin doublet is a quark doublet, the partial widths cannot be calculated without making additional approximations.

2.2.1 Muon Decay

The electron is a member of the least massive fermion doublet, therefore it is stable because energy and lepton number conservation forbid all decays. The muon is heavier than the electron but lighter than all hadrons, so the muon may decay via the diagram in Figure 2.1 only if the fermion doublet is the $(\nu_e\ e^-)$ doublet. The partial width for the decay mode $\mu^- \rightarrow e^-\overline{\nu}_e\nu_\mu$, calculated using the standard model with m_e set to zero (which simplifies the algebra without significantly altering the result) [18], is

$$\Gamma(\mu^- \rightarrow e^-\overline{\nu}_e\nu_\mu) = \frac{G_F^2 m_\mu^5}{192\pi^3}, \tag{2.1}$$

where G_F is the characteristic strength of the weak interaction. Since this decay mode is the only mode that contributes to muon decay, Equation 2.1 and the measured μ^- lifetime of 2.2×10^{-6} s [17] are used to determine the weak coupling constant G_F.

2.2.2 Leptonic Tau Decay

The τ^- is massive enough to decay either into leptons through the $(\nu_e\ e^-)$ or the $(\nu_\mu\ \mu^-)$ doublet, or into hadrons through the $(u\ d')$ doublet. The partial decay widths for the leptonic τ^- decays are calculated with the standard model in the same manner as the width for μ^- decay is calculated (Equation 2.1). This results in partial widths of

$$\Gamma(\tau^- \rightarrow e^-\overline{\nu}_e\nu_\tau) = \frac{G_F^2 m_\tau^5}{192\pi^3} \tag{2.2}$$

and

$$\Gamma(\tau^- \rightarrow \mu^-\overline{\nu}_\mu\nu_\tau) = 0.97 \cdot \frac{G_F^2 m_\tau^5}{192\pi^3}, \tag{2.3}$$

Decay Mode $\tau^- \rightarrow$	Predicted Branching Fraction (%)	Measured Branching Fraction (%)
$e^-\overline{\nu}_e\nu_\tau$	17.6	17.4 ± 0.5
$\mu^-\overline{\nu}_\mu\nu_\tau$	17.0	17.6 ± 0.6
$\pi^-\nu_\tau$	10.7	10.1 ± 1.1
$K^-\nu_\tau$	0.7	0.7 ± 0.2
$\rho^-\nu_\tau$	21.6	22.1 ± 1.4
$K^{*-}\nu_\tau$	1.2	1.7 ± 0.7
$K^-\nu_\tau(+neutrals)$	—	1.7 ± 0.4
$\tau^- \rightarrow \pi^-\pi^0\pi^0\nu_\tau$	—	6.0 ± 3.5
$\tau^- \rightarrow \pi^-\pi^0\pi^0\pi^0\nu_\tau$	—	3.0 ± 2.7
$\pi^-\pi^+\pi^-\nu_\tau$	—	7.1 ± 0.8
$\pi^-\pi^+\pi^-\pi^0\nu_\tau$	—	5.3 ± 0.8
$K^-\pi^+\pi^-(\pi^0)\nu_\tau$	—	0.2 ± 0.2
$K^-K^+\pi^-\nu_\tau$	—	0.2 ± 0.2
$5\pi^\pm\nu_\tau$	—	0.07 ± 0.03
$5\pi^\pm\pi^0\nu_\tau$	—	0.07 ± 0.03
B_1	—	86.5 ± 0.3
B_3	—	13.4 ± 0.3
B_5	—	0.15 ± 0.04

Table 2.3: Measured Branching Fractions of the τ^-

where the correction factor of 0.97 in Equation 2.3 is due to the mass of the μ^-. The partial widths in Equations 2.2 and 2.3 are combined with the measured total lifetime of the τ^- of $(2.8 \pm 0.2) \times 10^{-13}$ s [17] to obtain the predictions for the leptonic branching fractions $B(\tau^- \rightarrow e^-\overline{\nu}_e\nu_\tau)$ and $B(\tau^- \rightarrow \mu^-\overline{\nu}_\mu\nu_\tau)$ listed in Table 2.3.

2.2.3 Hadronic Tau Decay

It is more difficult to predict the partial widths for the decays of the τ^- into hadrons. The standard model is able to describe how the τ^- decays into a ν_τ and a quark-antiquark pair, but is unable to predict how the $\overline{u}$ and d' quarks combine to form hadrons (Figure 2.2). However, it is possible to make theoretical predictions for the hadronic branching fractions of the τ^- by making additional assumptions [19,1].

Decays into π^- and K^-

The branching fractions $B(\tau^- \rightarrow \pi^-\nu_\tau)$ and $B(\tau^- \rightarrow K^-\nu_\tau)$ are calculated using the measured π^- and K^- lifetimes. The decays of the π^- and the K^- proceed through the diagram in Figure 2.3. The strength of the coupling between the W^-

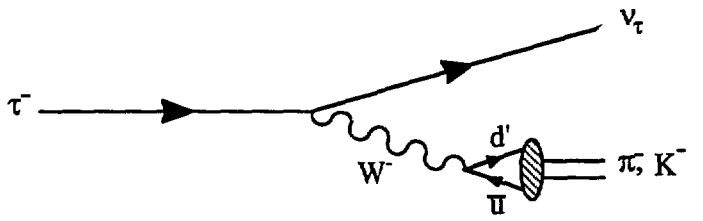

Figure 2.2: Diagram for Hadronic Tau Decay

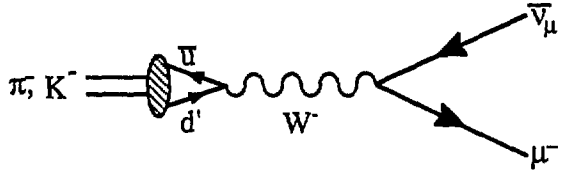

Figure 2.3: Diagram for Hadron Decay

and the π^- or K^- is obtained by measuring the partial width for $\pi^- \rightarrow \mu^-\overline{\nu}_\mu$ decays and $K^- \rightarrow \mu^-\overline{\nu}_\mu$ decays. This coupling strength, which is the same coupling strength represented in Figure 2.2, is used to compute the partial widths for the decays $\tau^- \rightarrow \pi^-\nu_\tau$ and $\tau^- \rightarrow K^-\nu_\tau$, then combined with the measured τ^- lifetime to predict the branching fractions $B(\tau^- \rightarrow \pi^-\nu_\tau)$ and $B(\tau^- \rightarrow K^-\nu_\tau)$ listed in Table 2.3.

Decays into ρ^- and K^{*-}

Predictions for the branching fractions $B(\tau^- \rightarrow \rho^-\nu_\tau)$ and $B(\tau^- \rightarrow K^{*-}\nu_\tau)$ are calculated using Figure 2.2, the same diagram that describes the decays $\tau^- \rightarrow \pi^-\nu_\tau$ and $\tau^- \rightarrow K^-\nu_\tau$. Unfortunately, it is impossible to measure the coupling of the W^- to the ρ^- and the K^{*-} by measuring their leptonic decay widths, as was done for the π^- and K^-, as the ρ^- and K^{*-} decay very rapidly via the strong interaction. However, the strength of the coupling between the W^- and the ρ^- can be determined using the conserved vector current hypothesis (CVC), which relates the W^--ρ^- coupling to the γ-$(\pi^-\pi^+)$ coupling. By using the cross section $\sigma(e^+e^- \rightarrow \gamma^* \rightarrow \pi^-\pi^+)$ to determine the γ-$(\pi^-\pi^+)$ coupling, the branching fraction $B(\tau^- \rightarrow \rho^-\nu_\tau)$ is calculated using the standard model and the measured τ^- lifetime [1]. This branching fraction is then multiplied by a Cabibbo suppression factor and a phase space factor to obtain the branching fraction $B(\tau^- \rightarrow K^{*-}\nu_\tau)$ [1]. The results of these theoretical predictions are quoted in Table 2.3.

Decays into $(3\pi)^-$ and $(4\pi)^-$

The branching fractions for decay modes that have more than two hadrons in the final state are more difficult or impossible to calculate, as it is difficult to measure the coupling of the W^- to the many hadron final state. However, isospin invariance is used to convert the measured branching fractions $B(\tau^- \to \nu_\tau \pi^- \pi^+ \pi^-)$ and $B(\tau^- \to \nu_\tau \pi^- \pi^+ \pi^- \pi^0)$ [2,20,21] into limits for the branching fractions $B(\tau^- \to \nu_\tau \pi^- \pi^0 \pi^0)$ [1] and $B(\tau^- \to \nu_\tau \pi^- \pi^0 \pi^0 \pi^0)$ [22]. These isospin arguments yield the relations

$$\frac{1}{4} \leq \frac{B(\tau^- \to \nu_\tau \pi^- \pi^0 \pi^0)}{B(\tau^- \to \nu_\tau \pi^- \pi^+ \pi^-)} \leq 1 \tag{2.4}$$

and

$$0 \leq \frac{B(\tau^- \to \nu_\tau \pi^- \pi^0 \pi^0 \pi^0)}{B(\tau^- \to \nu_\tau \pi^- \pi^+ \pi^- \pi^0)} \leq \frac{2}{3}. \tag{2.5}$$

Further arguments are used to limit the range of allowed values in Equations 2.4 and 2.5. The decay mode $\tau^- \to \nu_\tau \pi^- \pi^+ \pi^-$ is dominated ($> 80\%$) by the decay chain $\tau^- \to \nu_\tau A(1270)^- \to \nu_\tau \rho^0 \pi^- \to \nu_\tau \pi^- \pi^+ \pi^-$ as opposed to non-resonant $\pi^- \pi^+ \pi^-$ production [21]. If all $(3\pi)^-$ decays of the τ^- go through the $A(1270)^-$, the isospin prediction in Equation 2.4 becomes

$$B(\tau^- \to \nu_\tau \pi^- \pi^0 \pi^0) = B(\tau^- \to \nu_\tau \pi^- \pi^+ \pi^-). \tag{2.6}$$

A CVC argument similar to that used to predict the branching fraction $B(\tau^- \to \nu_\tau \rho^-)$ is used to predict the branching fraction $B(\tau^- \to \nu_\tau \pi^- \pi^0 \pi^0 \pi^0)$. In this case, the coupling of the W^- to the $\pi^- \pi^0 \pi^0 \pi^0$ system is related to the γ-$(\pi^- \pi^+ \pi^- \pi^+)$ coupling. The cross section $\sigma(e^+ e^- \to \gamma^* \to \pi^- \pi^+ \pi^- \pi^+)$ is used to determine the γ-$(\pi^- \pi^+ \pi^- \pi^+)$ coupling, and the branching fraction $B(\tau^- \to \nu_\tau \pi^- \pi^0 \pi^0 \pi^0)$ is then calculated using the standard model and the measured τ^- lifetime [1]. The results of these theoretical predictions are listed in Table 2.4.

Other Decays

The remaining decay modes for the τ^- fall into three main categories, those with more than 4 pions, those with a K^- (or K^{*-}) and additional hadrons, and those with η's in the final state. The predictions for these branching fractions are less reliable than the predictions for the branching fractions listed above, but all of these branching fractions are expected to be small so accurate predictions are not necessary. Therefore, the predictions for the branching fractions associated with these decay modes will be discussed in less detail than the previous predictions, and are all tabulated in Table 2.4.

It is impossible to calculate the branching fraction for τ^- decays into more than 4 pions, as the coupling of the W^- to the many pion system is not known. However, the branching fraction for decays with 5 charged pions has been measured [4], so the isospin relation

$$B(\tau^- \to \nu_\tau \pi^- 4\pi^0(\pi^0)) \leq \frac{9}{7} \cdot B(\tau^- \to \nu_\tau 5\pi^\pm(\pi^0)) \tag{2.7}$$

Decay Mode $\tau^- \rightarrow$	Predicted Branching Fraction (%) Total	One Prong
$\pi^-\pi^0\pi^0\nu_\tau$	7.1	7.1
$\pi^-\pi^0\pi^0\pi^0\nu_\tau$	1.0	1.0
$\pi^-\pi^0\eta\nu_\tau$	0.7	0.5
$\pi^-4\pi^0(\pi^0)\nu_\tau$	< 0.2	< 0.2
$\pi^-\eta\eta\nu_\tau$	< 1.5	< 0.8
$\pi^-\pi^0\pi^0\eta\nu_\tau$	< 0.5	< 0.4
$(K\overline{K})^-\nu_\tau$	< 1.8	< 1.2
$(K\overline{K}\pi)^-\nu_\tau$	< 0.5	< 0.3
$(K\pi\pi(\pi))^-\nu_\tau$	< 0.4	< 0.2

Table 2.4: Predicted Branching Fractions of the τ^-

can be used to predict the branching fraction for the analogous one prong decay modes [1].

There are many possible final states associated with the τ^- decay modes that involve a K^- (or K^{*-}) and additional hadrons, but all are Cabibbo suppressed analogs of the $\tau^- \rightarrow \nu_\tau(n\pi)^-$ decay modes. The predictions for these branching fractions are obtained using several methods [1]. Some predictions, such as the prediction for the decay mode $\tau^- \rightarrow \nu_\tau(K\overline{K})^-$, are obtained using the CVC hypothesis, while other predictions, such as the predictions for the decay modes $\tau^- \rightarrow \nu_\tau(K\overline{K}\pi)^-$ and $\tau^- \rightarrow \nu_\tau(K\pi\pi(\pi))^-$, are obtained using isospin considerations and the measured branching fractions $B(\tau^- \rightarrow \nu_\tau K^-K^+\pi^-)$ and $B(\tau^- \rightarrow \nu_\tau K^-\pi^+\pi^-(\pi^0))$ [23].

Several decay modes involving η's are possible. The decay mode $\tau^- \rightarrow \nu_\tau\pi^-\eta$ is forbidden, as this final state cannot couple to either the vector or the axial vector portion of the weak current. The prediction for $B(\tau^- \rightarrow \nu_\tau\pi^-\pi^0\eta)$ is obtained by assuming that the $\tau^- \rightarrow \nu_\tau(4\pi)^-$ decay mode is dominated by the $\rho(1600)^-$ meson. The branching fraction $B(\tau^- \rightarrow \nu_\tau\pi^-\pi^+\pi^-\pi^0)$ is combined with the branching fractions $B(\rho(1600)^- \rightarrow \pi^-\pi^+\pi^-\pi^0)$ and $B(\rho(1600)^- \rightarrow \pi^-\pi^0\eta)$ to obtain a prediction for the branching fraction $B(\tau^- \rightarrow \nu_\tau\pi^-\pi^0\eta)$. Limits on branching fractions such as $B(\tau^- \rightarrow \nu_\tau\pi^-\eta\eta)$ and $B(\tau^- \rightarrow \nu_\tau\pi^-\pi^0\pi^0\eta)$ are obtained from the measured branching fraction $B(\tau^- \rightarrow \nu_\tau 5\pi^\pm(\pi^0))$, isospin, and the inclusive branching fraction of the η into two charged pions [24, p.21].

2.3 Discussion

The existing measurements for the τ^- branching fractions, the theoretical predictions for these branching fractions, and the measured topological branching fractions B_1, B_3, and B_5 are summarized in Table 2.3. Note that all of these theoretical predictions are based on a τ^- lifetime of $(2.8 \pm 0.2) \times 10^{-13}$ sec [17].

The agreement between the predicted and measured branching fractions is excellent, as it should be, because the theoretical predictions are based on the firmly established tenets of the standard model, CVC, and isospin. However, the sum of these measured exclusive one prong branching fractions is $(68.9 \pm 2.0)\%$, while the inclusive one prong branching fraction B_1 is $(86.5 \pm 0.3)\%$. The existing measurements for decays involving more than one neutral meson [6] have been excluded from this sum because of the large uncertainty in these measurements (Chapter 1). The error on the sum of the exclusive branching fractions is computed by adding the individual errors in quadrature, which ignores the correlations between measurements. If the error is computed by scaling the error on the electron branching fraction, which is a reasonable estimate for the error if the measurements are strongly correlated, the value of the error is also 2.0%.

An obvious explanation for this difference between inclusive and exclusive branching fractions is that some of the one prong τ^- branching fractions have not yet been measured. Table 2.4 summarizes the predicted values for the τ^- branching fractions that have yet to be measured, as well as their expected contribution to the one prong final state. The predictions in Table 2.4 cannot be summed directly to obtain a theoretical estimate for the missing one prong branching fraction, as this would result in double counting. The limits on $B(\tau^- \rightarrow \nu_\tau \pi^- 4\pi^0(\pi^0))$, $B(\tau^- \rightarrow \nu_\tau \pi^- \eta\eta)$, and $B(\tau^- \rightarrow \nu_\tau \pi^- \pi^0 \pi^0_{ij})$ are all obtained from B_5, therefore only one of these branching fractions can contribute at the limit quoted in Table 2.4. Similarly, many of the predicted decay modes involving kaons contribute to the measured inclusive branching fraction $B(\tau^- \rightarrow \nu_\tau K^-(+neutrals))$ and so have already been included in the sum of measured branching fractions. Therefore, if the predicted branching fractions for these decay modes are summed without double counting and with the upper limits included in the sum at their maximum value, the additional contribution to the one prong branching fraction is 9.4%, barely half of the $(17.6 \pm 2.0)\%$ difference.

Most of the measured branching fractions listed in Table 2.3 have been measured by more than one experiment, so it is unlikely that the discrepancy between the inclusive and exclusive branching fractions is due to an incorrect measurement. Therefore, it seems likely that one (or more) of the theoretical estimates in Table 2.4 is incorrect. It is unlikely that the problem lies in the upper limits quoted in Table 2.4, as these upper limits are derived only from isospin considerations and the measured branching fractions of the η, and so are fairly reliable. In addition, the predicted contribution from these decay modes is small, and would have to increase by an order of magnitude to account for the discrepancy.

The prediction for $B(\tau^- \rightarrow \nu_\tau \pi^- \pi^0 \pi^0)$ has some potential for error. It is based on isospin considerations and the measured branching fraction $B(\tau^- \rightarrow \nu_\tau \pi^- \pi^+ \pi^-)$, and there is some disagreement among the recent high precision measurements of this branching fraction. These measurements are summarized in Table 2.5, where the weighted average and error are computed with the method used by the Particle Data Group [5, p.6]. However, these fluctuations are too small to account for the discrepancy.

Experiment	Measurement (%)
MAC [2]	7.7 ± 0.7
DELCO [20]	5.0 ± 1.0
Mark II [21]	7.8 ± 0.9
Average	7.1 ± 0.8

Table 2.5: Recent Measurements of $B(\tau^- \rightarrow \nu_\tau \pi^- \pi^+ \pi^-)$

The prediction for $B(\tau^- \rightarrow \nu_\tau \pi^- \pi^0 \pi^0 \pi^0)$ is based on the CVC hypothesis, which is also a firmly established principle, although not as firmly established as isospin. If the CVC prediction is ignored, isospin considerations can be used to place a limit of 3.5% on $B(\tau^- \rightarrow \nu_\tau \pi^- \pi^0 \pi^0 \pi^0)$, which is still not enough to account for the discrepancy.

The prediction most likely to be incorrect is the prediction for the branching fraction $B(\tau^- \rightarrow \nu_\tau \pi^- \pi^0 \eta)$. This prediction is based on the assumption of $\rho(1600)^-$ domination of the $(4\pi)^-$ system, but the support for this assumption is weak [25] and there is even some evidence against this assumption [6]. The confusion is compounded because the branching fractions of the $\rho(1600)^-$ are not firmly established [5, p.201], therefore the theoretical prediction for $B(\tau^- \rightarrow \nu_\tau \pi^- \pi^0 \eta)$ could be incorrect by an order of magnitude, which would account for the discrepancy.

Chapter 3

Detector

This chapter describes the equipment used to detect the decay products of tau leptons. The discussion begins with a general description of the detector system and ends with a detailed description of the elements that have the greatest significance to the analysis presented in this dissertation.

The tau leptons analyzed in this experiment are produced in $e^+e^- \rightarrow \tau^+\tau^-$ interactions at the PEP (Positron Electron Project) storage ring at the Stanford Linear Accelerator Center. PEP produces collisions at 29 GeV center of mass energy, with a spread in energy of about 200 MeV. A typical luminosity is 2.0×10^{31} $cm^{-2}sec^{-1}$, yielding a total $e^+e^- \rightarrow \tau^+\tau^-$ event rate of approximately 1 per 5 minutes.

3.1 PEP-4

The PEP-4 detector facility surrounds one intersection point at PEP. PEP-4 attempts to measure the momentum and particle type in as much of the 4π solid angle around the intersection point as possible with a now familiar barrel geometry. The system is cylindrically symmetric, with the axis of symmetry along the beam line. A side view of the detector system is shown schematically in Figure 3.1.

The PEP-4 detector system is broken into three major subsystems – the charged particle system (used to measure the trajectories of charged particles), the calorimeter system (used to measure photon energies and positions), and the muon system (used to identify muons). The charged particle system, composed of the Inner Drift Chamber (IDC), the Time Projection Chamber (TPC), the magnet coil, and the Outer Drift Chamber (ODC), is the subsystem located closest to the intersection point. It is surrounded by the electromagnetic calorimeter system, composed of the Hexagonal Calorimeter (Hex) and the Pole Tip Calorimeter (PTC), which are surrounded in turn by the muon identification system.

The main strength of the PEP-4 detector system is its ability to provide excellent particle identification and detection efficiency for both charged particles and photons over approximately 75% of the solid angle. Its main weakness is

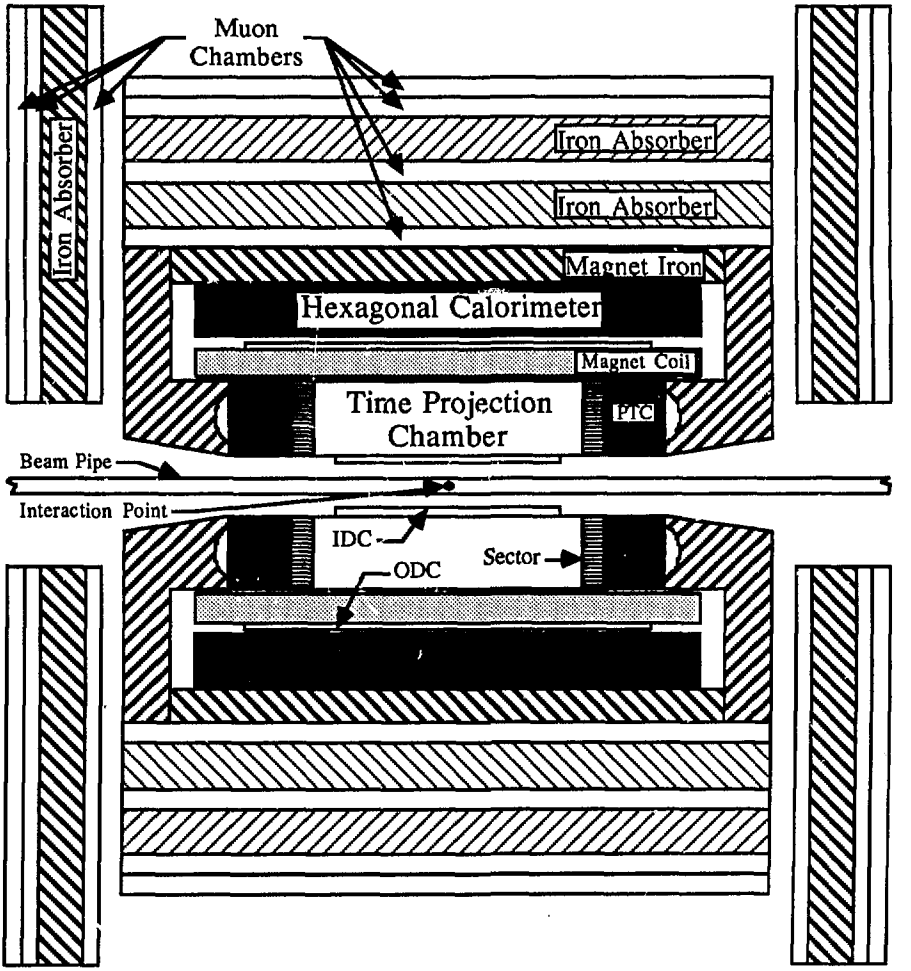

Figure 3.1: PEP-4 Detector System

relatively poor energy resolution.

3.1.1 Charged Particle System

Charged particles are detected by the Inner Drift Chamber (IDC), the Time Projection Chamber (TPC), the Outer Drift Chamber (ODC), and the magnet coil. The IDC and ODC are used almost exclusively to provide trigger information, while the TPC and the magnet measure the particle momentum and mass.

The IDC [26] is the active element closest to the intersection point. It is a cylindrical drift chamber 1.2 m long, with an inner radius of 14 cm. It has 4 axial layers with 60 sense wires per layer, successive layers of wires being staggered by half a cell spacing in azimuth. The IDC provides the trigger system with accurate timing information (30 ns), as well as a count of the number of tracks that point toward the intersection point. Unfortunately, no azimuthal information from the IDC is used in the trigger because portions of the IDC failed.

Surrounding the IDC is the Time Projection Chamber (TPC) [27], the central tracking detector for the PEP-4 facility. The TPC is drift chamber with an extremely long (1 m) drift distance, able to measure particle position (in 3 dimensions) and ionization rate simultaneously. The ionization trail deposited by a charged particle as it traverses the TPC volume is drifted axially toward the endcaps by a uniform electric field. Once the ionization reaches the endcaps, it is amplified on proportional wires, and both spatial and pulse height information are recorded. Physically, the TPC is a cylinder two meters long and one meter in radius, filled with 8.5 atm of 80% Argon – 20% Methane gas. This gas is contained at the inner radius by an aluminum pressure wall located just inside the IDC, by the magnet coil at the outer radius, and by the iron detector supports at the endcaps.

The TPC is surrounded by a solenoidal magnet that provides a 4.0 kG axial magnetic field parallel to the TPC drift direction. The coil package is made of aluminum, and is about 1.4 radiation lengths thick. Charged particles bend as they pass through the magnetic field, the radius of curvature proportional to the particle momentum. The magnetic field also limits the transverse dispersion of the ionization trail as it drifts toward the endcaps.

Attached to the outside of the magnet coil is the Outer Drift Chamber (ODC) [26] which, like the IDC, is used mostly for triggering, but also determines whether photons convert in the coil. The ODC is a cylindrical drift chamber 3 m long, with 3 axial layers of 216 sense wires each, successive layers being staggered by a half, then a quarter of a cell spacing in azimuth. The timing information from the ODC is not as good as the IDC, but it does retain the ability to identify tracks coming from the general direction of the interaction point.

3.1.2 Calorimetry

High energy photons are detected and their energy measured in the electromagnetic calorimeters that surround the charged particle detection system. The

Hexagonal calorimeters (Hex) measure most of the photons used in this analysis and provide trigger information, while the lead/proportional wire Pole Tip Calorimeters (PTC) are used primarily to measure luminosity.

Outside of the coil and the ODC are the six trapezoidal modules of the Hexagonal Calorimeter (Hex), which cover approximately 75% of the 4π solid angle around the interaction point [28]. Each module is 10.4 radiation lengths thick, 3.6 m long, and 1.8 m wide, and is composed of forty planes of Geiger cells sandwiched between lead sheets. Photons impinging on the Hex generate electromagnetic showers in the lead, which are then sampled by three sets of strip channels oriented at 60° to each other. Each channel is a half degree wide, giving the Hex good spatial resolution and two hit separation.

3.1.3 Muon System

The electromagnetic calorimeters are surrounded by iron interleaved with proportional chambers in order to detect muons [29]. There are three layers inside of 50 cm of iron in each endcap, four layers inside of 90 cm of iron in the barrel portion of the detector.

3.2 Time Projection Chamber

A charged particle, when traversing a medium, leaves a trail of ionization. This trail is used to determine the characteristics of the particle that cause it. The curvature and spatial location of the track determine the momentum of the particle, while the amount of ionization deposited (dE/dx) measures the particle's velocity. If a particle's velocity and momentum are both known, its mass, and thus its identity, can be inferred.

The TPC uses two parallel planes of proportional chambers (sectors) in conjunction with an axial electric field to detect this ionization trail (Figure 3.2). The uniform electric field drifts the trail at constant velocity through the TPC gas volume until it reaches the sectors, where the ionization is amplified and the position and arrival time are recorded. Cathode pads on the sectors give X and Y position information, while the arrival time supplies the Z position. Thus, the TPC has the ability to measure all three position coordinates of each point on the track simultaneously, which makes it fairly easy to reconstruct the track.

3.2.1 Electric Field

The drift field for the TPC is induced by placing a conducting mesh parallel to and centered between the two parallel proportional chambers. The endcaps are held at ground potential and the mesh is held at -75 kV, producing a axial electric field of 75 kV/m. The field is shaped by a stack of electrodes at the inner and outer radius of the drift volume. Constant voltages are maintained on these

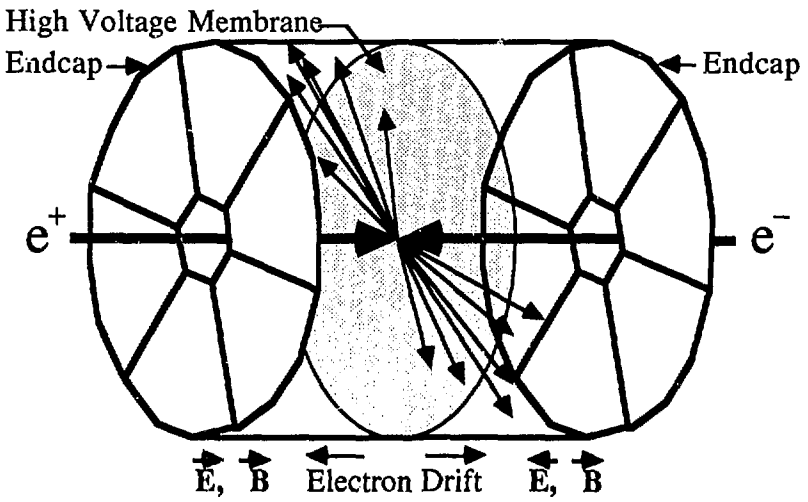

Figure 3.2: TPC Detector

electrodes via a series of precision resistors, reducing edge effects and forcing the electric field to be both axial and constant.

3.2.2 Magnetic Field

The magnetic field for the TPC is also aligned axially, and therefore parallel to the electric field. It is produced by a solenoidal coil, with edge effects minimized by shaped iron pole pieces at either end.

3.2.3 Sectors

The proportional chambers at the endcaps are divided into twelve identical segments (six per endcap) called sectors. Each sector is kite-shaped (Figure 3.3), extending from a radius of 20 cm to 100 cm and covering 60° in azimuth. Ionization is amplified by a proportional mode avalanche on 183 parallel sense wires strung perpendicular to the radial centerline. These sense wires are interspersed with field shaping wires to improve gain uniformity and reduce crosstalk. In addition, there are rows of 7.5 × 7.5 mm cathode pads under fifteen of the sense wires. The horizontal lines in Figure 3.3 represent the field and sense wires while the rows of squares represent the cathode pads. The signal that the avalanche induces on these pads determines the position of the track, while the signal that appears directly on the wires measures the amount of ionization.

Small gain variations cause substantial error in both position and ionization measurements, so care is taken to make the gain as uniform as possible. The sectors are water cooled to control temperature, as a 1° C temperature change causes the gain to vary by 3%. The electronics is calibrated to 1% accuracy

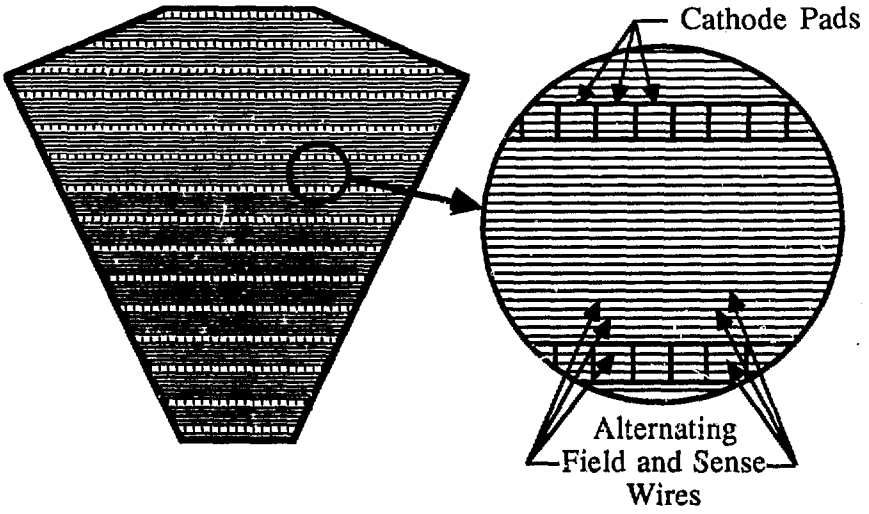

Figure 3.3: TPC Sector

by electronically pulsing each amplifier with a precision voltage source and by directly measuring wire gain using Iron-55 sources. Both positions and gains are corrected in later analysis stages for temperature variations and gradients, drift velocity variations, electron capture, pressure changes, sense wire voltage variations, and electrostatic distortions. The end result is a dE/dx resolution of $(3.65 \pm 0.2)\%$ and a momentum resolution of $(\sigma_p/p)^2 = (.06)^2 + (.035p)^2$ (GeV/c).

Simultaneous measurements of momentum and ionization rate determine the particle type. Figure 3.4 is a plot of dE/dx versus momentum, showing bands from electrons, pions, kaons, and protons passing through the TPC along with the theoretical prediction for each particle type. A chi-squared is calculated for each particle type based on both momentum and dE/dx (and their respective resolutions), and the values of chi-squared from these four mass hypotheses compared to determine the particle type. Individual particles are not always identified unambiguously because there are regions where the bands overlap, so the chi-squared values are used in different ways depending on the analysis. For example, accepting all tracks with $\chi^2_{electron} < 9.0$ selects electrons with high efficiency, but results in a sample that contains a large amount of hadronic background. Requiring $\chi^2_{electron} < 4.0$ and $\min(\chi^2_{pion}, \chi^2_{kaon}, \chi^2_{proton}) > 9.0$ yields a nearly pure electron sample, but has comparatively low electron finding efficiency.

3.3 Hexagonal Calorimeter

The Hexagonal Calorimeter (Hex) is the primary detector of photons in this analysis. It does this by forcing the high energy photon to undergo an electro-

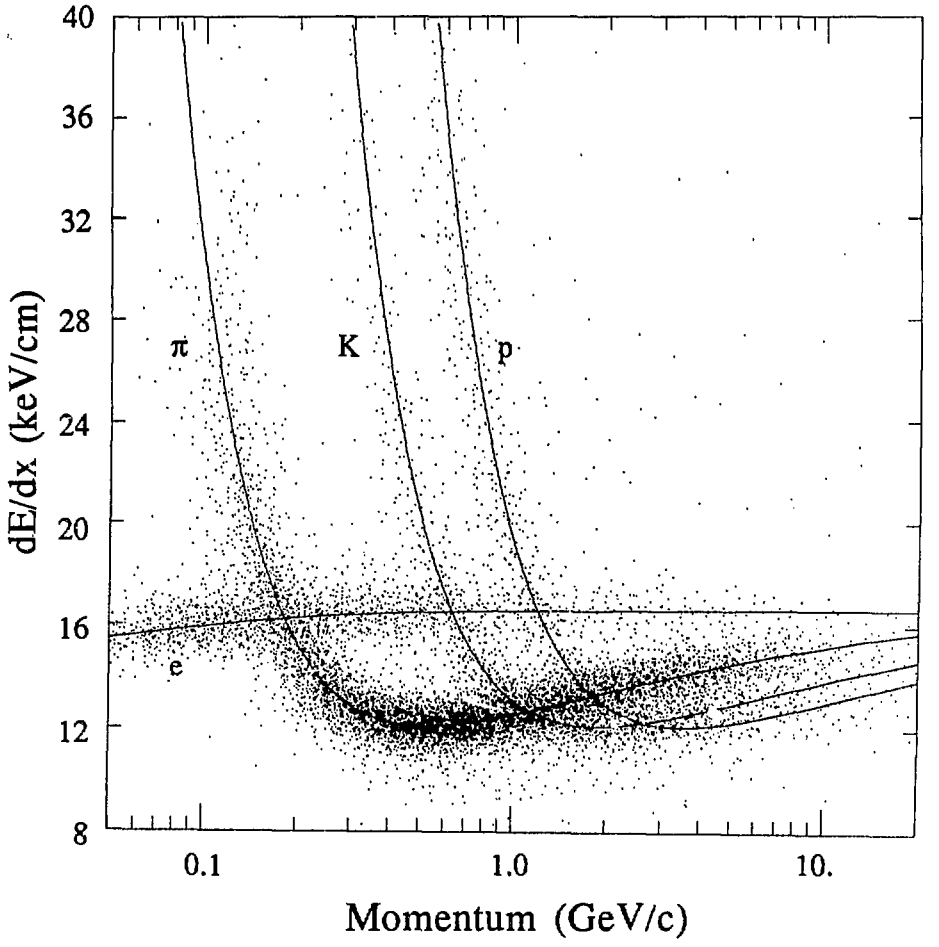

Figure 3.4: dE/dx vs. Log(Momentum)

magnetic shower. Sufficient material is placed in the path of the incoming photon so that it converts into an electron-positron pair. The electron and positron each emit a high energy bremsstrahlung photon, which then convert into an electron-positron pair, and this process continues until all of the initial photon energy is used up creating electrons, positrons and low energy photons. The energy of the incident photon is related (nearly linearly) to the number of resulting electrons and positrons. Since electrons and positrons are electrically charged, they are observed in the calorimeter via their ionization trails. Approximately 20% of the photons convert into an electron-positron pair in the 0.2 radiation length pressure wall in front of the TPC and are reconstructed by measuring the resulting pair of tracks in the TPC.

3.3.1 Modules

The Hex is a system of six identical calorimeter modules. Each module is a stack of forty layers of material (to provide a medium for the electromagnetic shower to occur in) interleaved with forty layers of Geiger mode detectors to sample the shower. Each layer is a laminate made up of a 0.056 in thick lead sheet (to provide maximum density for the shower) encased on both sides with 0.032 in of fiberglass (structural support and electrical insulation), then coated with a 0.005 in aluminum foil (electrical conductivity). On one side of each laminate is a plane of parallel sense wires spaced 5 mm apart, woven together with nylon filaments spaced 10 mm apart to form Geiger cells 0.5 cm^2 in area. Ceramic or fiberglass spacers glued to each laminate support the wire/nylon mesh and maintain a uniform 6 mm gap between laminates when they are stacked. High voltage is supplied to each layer independently, so individual layers may be turned off if problems (e.g. broken wires) develop. A laminate, with its wire plane attached, is shown in Figure 3.5.

The laminates are stacked on a one inch thick aluminum plate, then attached to the plate via a grid of 0.25 in diameter threaded rods on 28 cm centers. This stack is enclosed by gas cover of one eighth inch aluminum and sealed with Viton gaskets. An assembled module is shown in Figure 3.6.

The aluminum foil on each laminate is grooved to form parallel strips oriented at 60° angles to the wires – +60° on one side of the laminate, −60° on the other side. The strips are variable width, with the intent that each strip subtend the same solid angle around the interaction point as the strip in front of it. However, the strips actually point approximately 1 cm in front of the interaction point because of a design error, but this is easily corrected in the analysis. Similarly, sense wires within the same gap are ganged together to subtend the same solid angle as the wire gang in front of them.

The strips (and wires) are joined electrically to form two submodules in depth. The strips in the front 27 layers that subtend the same solid angle are combined to form 196 channels, each subtending a 10 mr arc, while the front 27 layers of wire groups form 128 channels subtending an 8 mr arc each. The rear 13 layers are also grouped together, each channel subtending twice the angular width as

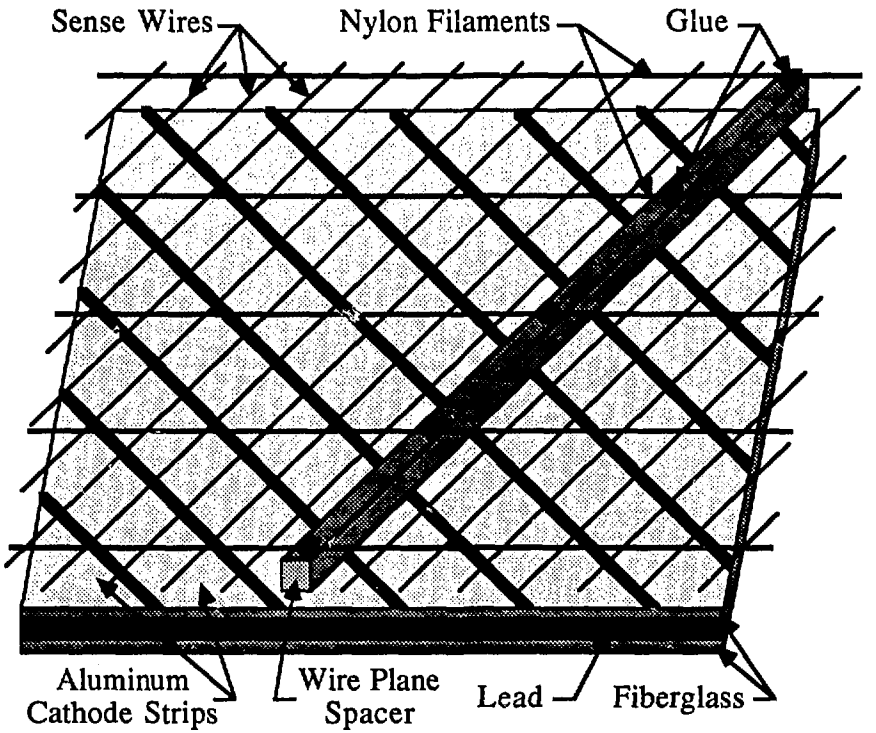

Figure 3.5: Hex Laminate

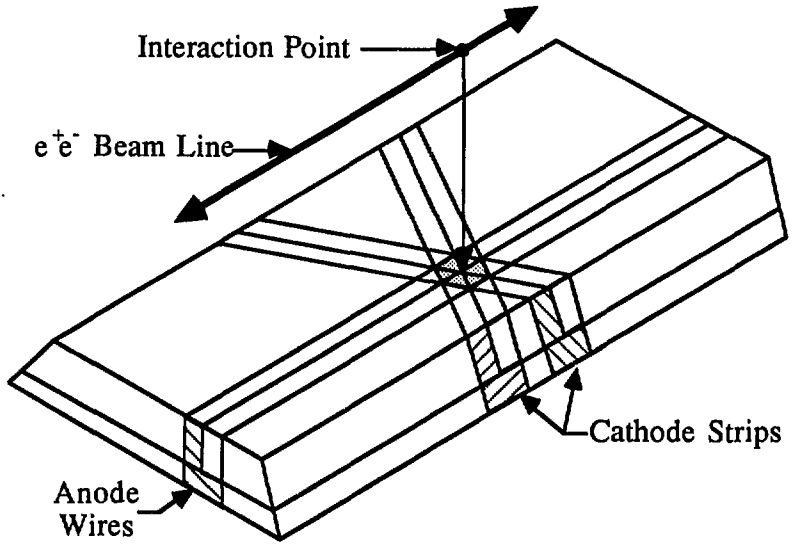

Figure 3.6: Hex Module

the corresponding channel in the front submodule.

3.3.2 Geiger Cells

The Hex uses a Geiger discharge to measure electrons and positrons passing through it. A potential of +1300 V is placed on the 0.02 mm diameter gold plated tungsten sense wires that operate in one atmosphere of 96% Argon – 4% Ethyl Bromide. A charged particle passing near a wire starts an avalanche on the wire that propagates along the wire. The 0.125 mm diameter nylon filaments that cross the wires every 10 mm stop the propagation the avalanche, and the sense wire collects the electrons liberated during the avalanche. The charge collected by the sense wire is roughly constant, depending only on the gas, high voltage, and Geiger cell geometry, and not on the initial amount of ionization deposited in the cell. The charge collected on the wire induces an equal (within 1.5%) charge that is evenly shared between the cathode planes on either side of the wire. Both the calibration scheme and the pattern recognition algorithm rely upon this charge matching.

The Geiger mode discharge has several advantages over proportional mode. The signal is large ($\sim$ 50 pC per cell), so we do not need preamplifiers on the detector, simplifying the electronics and making them more reliable. All cells produce the same (large) charge when they fire, so the Hex obtains the signal to noise ratio found in digital systems. It is easy to see a single cell firing in a module containing over 5 million cells, a fact used when calibrating. Finally, the Geiger mode is immune to ionization fluctuations caused by path length variations and Landau fluctuations since the charge released is independent of initial ionization.

The main disadvantage of the Geiger mode is that it is impossible to determine if more than one charged particle passes through an individual cell, but this does not significantly degrade the performance of the Hex for photon energies below 7 GeV.

3.3.3 Electronics

The charge collected from the 4608 wire and strip channels are directly transmitted to the electronics house via 35 m coaxial cables, where they are transformer coupled to charge sensitive amplifiers. The amplifiers have two stages, a fast (100 ns rise time) stage whose output goes both to the trigger system and to the input of a 2.5 μs peaking time shaping amplifier. The shaping amplifier output is sampled, then digitized by a 9 bit ADC that achieves a 4095:1 (12 bit) dynamic range by using a non-linear clock, and read out by an online data acquisition computer.

3.3.4 Calibration

The electronics is calibrated using an electronic test pulsing system. Each channel is pulsed with a precision voltage source at a variety of amplitudes, reducing channel to channel electronic gain variations to about 1%.

Since Geiger discharges are measured capacitively on the strip channels, strip to strip variations in capacitance result in channel to channel gain variations. These variations due to chamber capacitance are removed using charge conservation, that is, by demanding that the amount of charge measured on the anode wires is the same as the charge induced on the cathode strips. We collect events having a single particle hitting a module, and calculate the asymmetry $R = (A-C)/(A+C)$, where A and C are the measured charge on the anode and cathode channels. The gain of each channel is then corrected by a multiplicative factor to minimize the sum (over all events) of R^2. This reduces the 8% initial variations due to chamber capacitance to 1.5%.

Finally, local variations in Geiger gain are removed by measuring the pulse height produced by a single Geiger cell firing. Figure 3.7 shows the low amplitude output of an anode channel, summed over many events. A series of evenly spaced peaks corresponding to up to six Geiger cells firing is clearly seen. Variations in the spacing between peaks correspond to variations in gain that are corrected, resulting in an overall chamber uniformity (including electronics, chamber capacitance, and Geiger gain variations) of about 2%.

3.3.5 White Smoke

Unfortunately, a chemical reaction between Ethyl Bromide (a component of the chamber gas) and aluminum (the gas enclosure) crippled one of the six modules for the entire run cycle and another for about half of the run cycle. Aluminum and Ethyl Bromide combine to form Aluminum Bromide, an anhydrous white

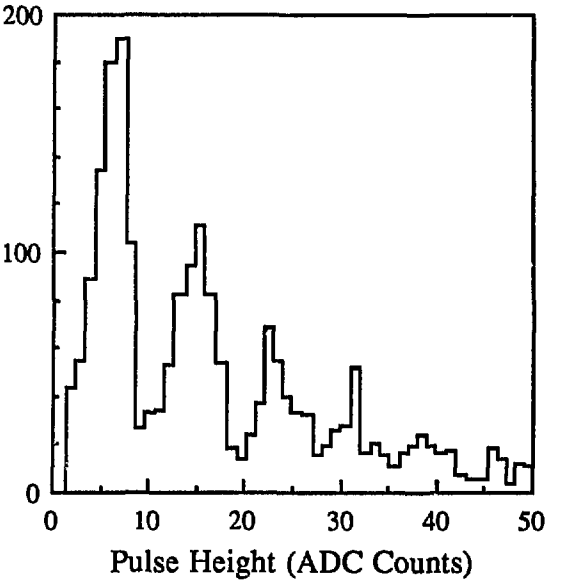

Figure 3.7: Hex Geiger Cell Structure

powder that reacts violently with humid air [30]. This reaction is difficult to initiate, but is autocatalytic, so modules that ran perfectly for months were destroyed in one day.

3.4 Trigger System

While the electron and positron beams cross every 2.45 μs, interactions that are measurable in our detector occur at an average rate of one every 10 seconds and $\tau^+\tau^-$ events occur approximately once every 5 minutes. If the data from the detector were collected on each beam crossing, the data acquisition system would be overwhelmed, so a trigger system is necessary to decide on an crossing by crossing basis if an interesting interaction took place. A very nice description of the overall charged particle trigger system is given in Bill Gary's doctoral dissertation [31, p. 83].

3.4.1 Overview

The trigger decision-making process is divided into three parts, the pretrigger, the trigger, and preanalysis. The pretrigger is a very fast (and very crude) decision that determines on each crossing if there is any possibility that an interaction occurred. If the pretrigger decides that an interaction may have taken place, it starts the trigger system and prevents the rest of the analog electronics from resetting, which it normally does to prepare for the next beam crossing. The

trigger waits for the ionization to drift to the TPC endcaps, then decides, with much better accuracy than the pretrigger, if an interaction was likely. If the trigger accepts an event, the analog electronics is read out by the online data acquisition computer, then is analyzed by preanalysis, a software verification of the hardware trigger. If the interaction is accepted by preanalysis, it is written to data tape.

3.4.2 Pretrigger

There are two categories of pretriggers, charged and neutral. The charged pretrigger looks for hits in the IDC pointing toward the beam interaction point that are synchronous in time with the beam crossover. Additional aligned hits in either the ODC or the TPC endcaps are required to ensure that the tracks generating the pretrigger penetrate to large radius.

The neutral pretrigger looks for energy deposit in either of the calorimeters (Hex or PTC) synchronous with the beam crossover time. The output from the fast portion of the Hex analog electronics is summed over all electronics channels, resulting in a signal with a rise time of 500 ns and a height proportional to the electromagnetic energy deposited in the calorimeter (500 mV/GeV). The Hex pretrigger requires this signal to be above the voltage corresponding to an energy of 500 MeV.

The summed Hex signal is also used to extract beam time synchronization information. The timing is done with a constant fraction discriminator rather than a leading edge discriminator to obtain timing information that is independent of pulse height over a large dynamic range (300 MeV to 30 GeV). We measure a peak of 50 ns full width centered around beam crossover time, but require that the timing signal from the Hex fall within merely ± 100 ns of the beam crossover time. Thus, the requirement for a Hex pretrigger is energy deposit of 500 MeV occurring within a 200 ns window around beam crossover time.

3.4.3 Trigger

Like the pretrigger, the trigger is divided into charged and neutral components. However, there are more subdivisions in the trigger system than in the pretrigger, including a trigger that combines charged and neutral information.

The main charged particle trigger is based on the TPC and known as the two ripple trigger. When a charged pretrigger occurs, this trigger looks for two (or more) charged tracks that point toward the origin and are separated by a minimum of 60° in azimuth. It is called a ripple trigger because of the method it uses to tell if the track points toward the origin. The TPC drift volume is divided into 64 time slices, corresponding to Z position, and groups of 8 wires that divide the TPC into 24 bands in radius. A hit at any radius at any time initiates a search for another hit at smaller radius and later time, the correlation between time and radius given by a straight line from the initial hit to the beam intersection point. If another hit is found at this smaller radius and later time,

it initiates a search for the next point in the line toward the origin. Thus, a charged track emanating from the origin appears as successive points rippling in from large radius to the origin. This trigger is excellent for multi-hadron events, having both high efficiency and low background rate. However, since both the pretrigger and trigger become less efficient with low charged particle multiplicity, this trigger is only about 87% efficient for $\tau^+\tau^-$ events.

There is one neutral trigger that uses only the Hex, a total energy trigger. A Hex trigger is generated if there is more than 2 GeV of electromagnetic energy in the Hex along with a neutral pretrigger. No explicit beam time synchronization is required to generate a trigger since beam synchronization is required in the pretrigger. This trigger is quite efficient ($> 99\%$), but suffers from a high cosmic ray background, forcing the high energy threshold.

The most effective trigger for the $\tau^+\tau^-$ event sample is a trigger that uses both charged and neutral components. This trigger extends the high trigger and pretrigger efficiency of the Hex to lower energies by using a portion of the charged particle trigger to reject cosmic rays. It requires one charged track pointing toward the origin (i.e. one ripple) along with greater than 750 MeV electromagnetic energy in the Hex, and allows either a charged or neutral pretrigger. Its efficiency for triggering on $\tau^+\tau^-$ events containing more than 750 MeV electromagnetic energy (which most do) is better than 99%.

3.4.4 Preanalysis

Preanalysis is a software verification of the hardware trigger, imposed after the event is read out by the online data taking computer. Events triggered by the charged particle trigger are required to pass the "charged preanalysis", while neutral triggers must pass the "neutral preanalysis". Events triggered by both charged and neutral triggers (or the mixed charged and neutral trigger) must pass either the charged or neutral preanalysis. Events that fail preanalysis are not written onto data tape.

Charged preanalysis is described in detail in Bill Gary's doctoral dissertation [31, p. 103]. It uses more detailed trigger information to determine that tracks generating a ripple actually intersect the beam interaction point in the Z direction, and uses a portion of the pad data from the TPC to require that tracks do not miss the origin in the radial direction.

Neutral preanalysis utilizes four cuts: timing, minimum energy, energy asymmetry, and shower width. The timing signal from the constant fraction discriminator is digitized and compared to the beam crossover time. A tighter timing cut is applied in preanalysis (125 ns) than in the hardware (200 ns). A minimum of 100 MeV energy deposit is required in the Hex, and must be distributed evenly between the anode and cathode channels ($(A - C)/(A + C) < 60\%$). Finally, a cut is placed on shower width to reject cosmic rays that strike a module from the side.

Chapter 4

Photon Reconstruction

Having described the physical construction of the Hex and TPC, the methods used to reconstruct photons in these detectors are discussed. Monte Carlo simulations of the Hex and the TPC are necessary to determine the performance of the photon reconstruction algorithms, so a description of the Monte Carlo simulations is also included.

4.1 Hex Photon Reconstruction

The task of the reconstruction algorithm is to infer the energy and position of the particles incident on the Hex from the output of the Hex electronics. Charged particles that do not interact in the Hex, such as muons, pions, kaons, and protons, typically fire a single Geiger cell in each layer that they traverse, while electrons and photons cause electromagnetic showers that fire many Geiger cells. Therefore, the relation between incident particle energy and number of cells in a shower depends on the incident particle type. The TPC is available to measure the momentum of charged particles so the Hex assumes that all incident particles are photons.

The algorithm for photon reconstruction in the Hex is divided into three steps: pattern recognition, energy assignment, and photon selection. Pattern recognition converts the output of the Hex electronics into spatially located Geiger discharges (known as clusters) and measures the number of Geiger cells associated with each cluster. Energy assignment is an algorithm that assigns energy to each cluster based (primarily) on the number of Geiger cells associated with the cluster. Photon selection rejects clusters that are poorly measured or not associated with photons.

4.1.1 Pattern Recognition

When a Geiger discharge occurs in the Hex the electronics records three projections of the discharge, the two cathode views and the one anode view. Most events contain several particles, each one initiating many Geiger discharges, so each view contains a superposition of projections. Figure 4.1 displays two events

as seen by the Hex, where the rectangle represents the active area of a Hex module and the parallel lines represent the signal in each electronics channel. The angle of these parallel lines corresponds to the direction sampled by each view, while the length of each line is proportional to the square root of the number of Geiger cells measured in that channel. Note that the Geiger cells are ganged together in depth, so no depth information is displayed. The pattern recognition algorithm must use these three views to locate the position of each shower and find the number of Geiger cells associated with each shower. Pattern recognition is simple in the Bhabha event shown in Figure 4.1(a), but becomes more difficult with increasing particle multiplicity and decreasing two hit separation, as shown by the multihadron event in Figure 4.1(b).

The pattern recognition algorithm reconstructs events by first finding peaks in each of the three views (1-D clusters), then searching for a placement of Geiger cells on the surface of the Hex (2-D clusters) that reproduces the data seen in each of the three views. This algorithm fits all clusters within a module simultaneously, enabling it to resolve overlapping clusters. Since the Hex electronics measures the charge liberated by the Geiger discharge and this charge is linearly proportional to the number of Geiger cells that fire (Section 3.3.2), the pattern recognition algorithm computes the number of Geiger cells in units of charge.

Clusters in One Dimension

The object of cluster finding in one dimension is to convert charge in electronics channels in one view into localized clusters. A cluster is defined as group of adjacent channels whose contents are characterized by three quantities: position, amplitude, and width. The 1-D cluster finding is conducted independently for each view in each module, resulting in eighteen lists (six modules, three views per module) of clusters in one dimension.

Before cluster finding in one dimension begins, the output of the Hex electronics is converted into a suitable form. Each electronics channel is corrected for electronics gain and chamber capacitance as described in Section 3.3.4 to find the true amount of charge seen by that channel. In addition, the contents of the electronics channels from the rear section of the Hex are combined with the corresponding channels in front section because the rear section is too thin in depth to contain enough information to do independent pattern recognition.

The algorithm first finds the channel with the greatest charge in a view, then parameterizes the charge in that channel and the two adjacent channels to an exponential shower shape with three free variables: center, height, and exponential slope. This procedure is iterated until a maximum of 3 cells (equivalent to about 20 MeV) or less remains in any view. The 1-D clusters in this view are then refined by performing a simultaneous fit to all channels in a view using a superposition of exponential shower shapes.

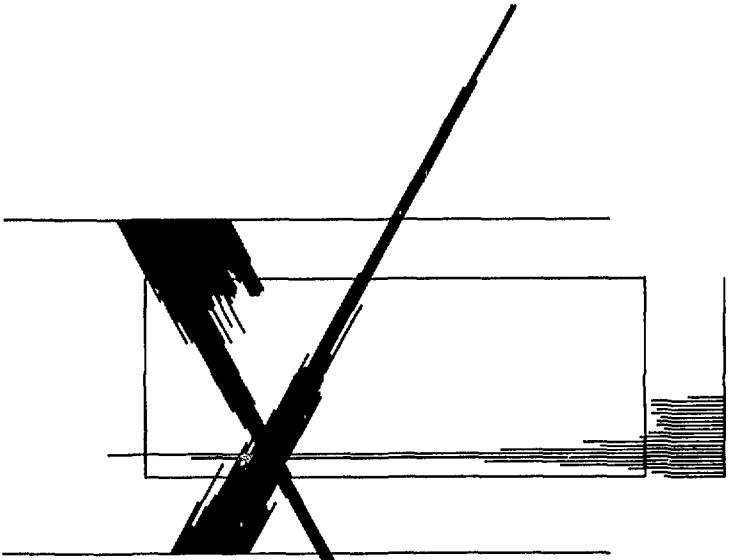

(a) Bhabha Event

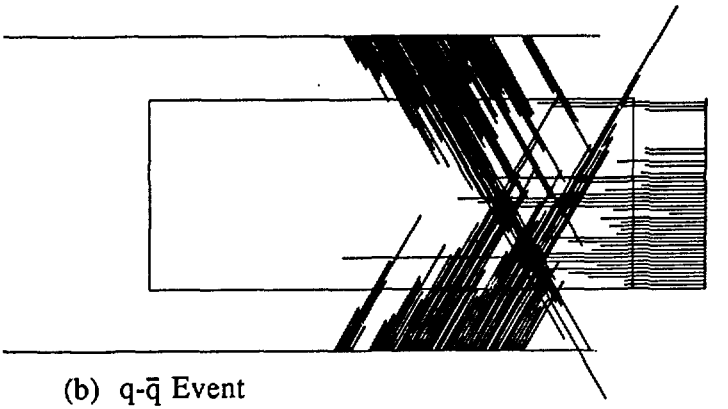

(b) q-$\bar{q}$ Event

Figure 4.1: Hex Events

Clusters in Two Dimensions

The object of cluster finding in two dimensions is to combine the three projections of a shower (i.e. 1-D clusters) into a single 2-D cluster. A simultaneous fit to all clusters within a module is done to resolve ambiguities caused by overlapping showers.

The center of one cluster in one cathode view is combined with the center of a cluster in the other cathode view to intersect at a unique point on the surface of the calorimeter module. This point is projected onto the anode view, and if a 1-D cluster in the anode cluster list is found near the point, the point on the surface is listed as a 2-D cluster candidate regardless of the charge of any of the clusters. The charge assigned to this 2-D candidate is the average number of ADC counts in the three clusters, and the process is iterated until all possible candidates are found.

This list of 2-D candidates contains many fake combinations caused by accidental overlap, and many of the correct combinations have incorrect charge assignments due to overlap with another cluster in one of the three views, but it should contain all of the correct combinations. The list is purged of false combinations and the charge of the correct combinations is refined using an iterative chi-squared fit based on the requirement that a 2-D cluster produce equal charge projections onto all three views. All 2-D clusters in a module are assigned charges as described in the preceeding paragraph, which then predict charges for the individual 1-D clusters. The difference between the predicted and measured charge is computed for all 1-D clusters, and the charge of the 2-D clusters are simultaneously adjusted to minimize this difference. Combinations assigned a very small or negative charge are labeled as fakes and removed from the list of 2-D candidates. The charges of the 2-D clusters are again adjusted to better reproduce the 1-D clusters, and the charge adjustment and fake removal process continues until no further adjustment is necessary.

Finally, the charge of each cluster is converted to number of Geiger cells using the method described in Section 3.3.4, then adjusted to compensate for missing layers, and the location of the cluster is computed. Two dimensions are given by the position of the 2-D cluster on the surface of the module; the center (in depth) of the front section of the module is assigned as the third dimension as all Geiger cells are ganged together in depth.

4.1.2 Energy Assignment

The task of the energy assignment algorithm is to infer the energy of each particle hitting the Hex from the size of the signal it produces. The relation between the particle energy and the number of Geiger cells depends on the particle type. For example, a hadron that does not shower produces a much smaller signal than an electron of the same energy. This analysis uses the Hex only to measure photons, therefore the energy assignment algorithm assumes that all clusters are due to incident photons.

The ideal way to determine the relation between incident photon energy and the number of Geiger cells that fire is to bombard the Hex with photons whose energy is known, then measure the response of the Hex. However, there is no suitable photon source, so electrons measured by the TPC are used to measure the response of the Hex to an electromagnetic shower, then the EGS [32] electromagnetic shower Monte Carlo described in Section 4.3 is used to make small corrections for the difference between showers initiated by electrons and photons.

There are three ways that the initial photon energy can be dissipated: it can be deposited in the Hex calorimeter module ($E_{Deposit}$), it can leak out of the back of the module ($E_{Leakage}$), or it can be lost in the 1.4 radiation length magnet coil in front of the Hex (E_{Loss}). In general, each process dissipates some energy, so:

$$E_{Initial} = E_{Deposit} + E_{Leakage} + E_{Loss} \; . \tag{4.1}$$

Pattern recognition provides the number of Geiger cells that fire, so the real purpose of the energy assignment algorithm is to provide three independent quantities – $E_{Deposit}$, $E_{Leakage}$, and E_{Loss} – as a function of the number of Geiger cells.

There are slight differences between electromagnetic showers initiated by photons and showers initiated by electrons, so Equation 4.1 corresponds to one equation for each species, or

$$E_{Initial} = E^{\gamma}_{Deposit}(cells) + E^{\gamma}_{Leakage}(cells) + E^{\gamma}_{Loss}(cells) \tag{4.2}$$

and

$$E_{Initial} = E^{e}_{Deposit}(cells) + E^{e}_{Leakage}(cells) + E^{e}_{Loss}(cells). \tag{4.3}$$

The EGS [32] Monte Carlo is used to determine the functions $E^{\gamma}_{Leakage}(cells)$ and $E^{\gamma}_{Loss}(cells)$, but this calibration scheme assumes that $E^{\gamma}_{Deposit}(cells)$ is equal to $E^{e}_{Deposit}(cells)$, which allows the function for $E_{Deposit}(cells)$ to be measured with electrons and positrons. All three functions are position dependent, but the following description ignores the position dependence for clarity.

The first function that is measured is $E_{Deposit}(cells)$. The first step in measuring this function is to determine how much energy, on average, is lost in the coil or leaks out the back of the calorimeter as a function of incident electron momentum ($E^{e}_{Leakage}(p_e)$ and $E^{e}_{Loss}(p_e)$). These functions are obtained using the EGS Monte Carlo to simulate showers in the coil and the calorimeter module.

Next, the TPC and the Hex are used to collect a very pure sample (0.1% contamination) of electrons and positrons in the momentum range 0.5 to 5 GeV/c. The momentum of each track is measured by the TPC while the Hex measures the number of Geiger cells that the track fires. Hadronic background is rejected by requiring that $\chi^2_{electron} < 2.0$ and $\chi^2_{hadron} > 4.0$ in the TPC and that greater than 60 Geiger cells (corresponding to about 350 MeV) fire in the Hex.

The function $E_{Deposit}(cells)$ is measured with these electrons and Equation 4.3, which is rewritten as

$$E_{Deposit} = E_{Initial} - E^{e}_{Leakage}(p_e) - E^{e}_{Loss}(p_e) \; . \tag{4.4}$$

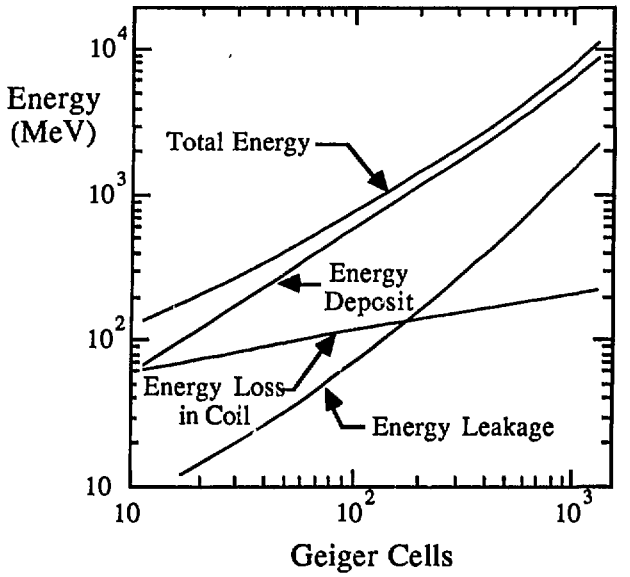

Figure 4.2: Hex Energy Calibration

Since $E_{Initial}/c$ is equal to the measured electron momentum p_e, Equation 4.4 is used to plot the number of Geiger cells that fire as a function of energy deposit. This plot is fit to find the first of the three necessary functions: $E_{Deposit}(cells)$ (Figure 4.2).

The next function fit is $E^{\gamma}_{Loss}(cells)$. The EGS Monte Carlo is run again to determine $E^{\gamma}_{Loss}(p_\gamma)$, the average energy loss in the coil as a function of incident photon energy. It is then necessary to change the independent variable, converting $E^{\gamma}_{Loss}(p_\gamma)$ into $E^{\gamma}_{Loss}(cells)$. The conversion takes place in two steps; incident energy is first converted to energy deposit, then energy deposit is converted to number of Geiger cells. Incident energy is converted to energy deposit using the photon analogy of Equation 4.4,

$$E_{Deposit} = E_{Initial} - E^{\gamma}_{Leakage}(p_\gamma) - E^{\gamma}_{Loss}(p_\gamma) \; . \tag{4.5}$$

Again, $E_{Initial}/c$ is equal to the photon momentum p_γ, so Equation 4.5 enables $E^{\gamma}_{Loss}(p_\gamma)$ to be converted to $E^{\gamma}_{Loss}(E_{Deposit})$. The function for $E_{Deposit}(cells)$ is inverted to obtain $Cells(E_{Deposit})$, which is then used to convert $E^{\gamma}_{Loss}(E_{Deposit})$ into the second necessary function: $E^{\gamma}_{Loss}(cells)$ (Figure 4.2).

The function for $E^{\gamma}_{Leakage}(cells)$ is obtained by running EGS to determine the average leakage as a function of incident photon energy $E^{\gamma}_{Leakage}(p_\gamma)$, then using the above method to convert incident energy to Geiger cells (Figure 4.2).

ODC Tagging

The coil is 1.4 radiation lengths thick, so about two-thirds of the incident photons begin to shower in the coil. For those photons that start to shower in the coil, the correct energy reconstruction formula is:

$$E_{Initial} = E_{Deposit} + E^{\gamma}_{Leakage} + E^{\gamma}_{Loss} , \tag{4.6}$$

but the E^{γ}_{Loss} term should not be added to those photons that pass through the coil without interacting. The ODC is between the coil and the Hex, so photons that convert in the coil are tagged by the hits they produce in the ODC, and the energy loss contribution is adjusted accordingly.

Wires in the ODC that fire are divided into two categories, those that have charged tracks identified by the TPC pointing towards them and those not associated with charged tracks. The number of each type of ODC hit, associated and non-associated, within three degrees in azimuth of the Hex cluster are counted. Hex clusters are divided into three categories, those with two or more non-associated ODC hits in the six degree window around the cluster (shower in the coil), those with less than two ODC hits of any kind in front of it (no shower in the coil), and those with two or more track associated hits (ambiguous). Clusters tagged as showering in the coil are assigned the full E^{γ}_{Loss}, clusters tagged as not showering in the coil are assigned an E^{γ}_{Loss} of zero, and those tagged as ambiguous are assigned two thirds (i.e. the fraction of photons that convert in the coil) of the normal E^{γ}_{Loss}.

4.1.3 Photon Selection

Not all clusters in the Hex are caused by photons. Charged tracks fire Geiger cells as they pass through the calorimeter, and pattern recognition routinely produces fake or badly measured clusters. Therefore, a variety of cuts are applied to purge non-photons and poorly reconstructed photons. The effect of each cut is checked with the π^0 peak in the $\tau^+\tau^-$ event sample – a cut is not used if a π^0 peak is visible in the γ-γ invariant mass combinations that it rejects.

Two cuts reject clusters due to charged tracks. Tracks identified by the TPC are extrapolated to the point where they intersect the Hex, and any cluster within 7 cm of that point is rejected. Energy deposit as a function of depth in the calorimeter is used to reject particles that are not incident nearly perpendicular to the surface of the Hex. Hadrons deposit energy uniformly in depth, so normally incident hadron clusters typically have two thirds of their Geiger cells in the front section, and electromagnetic showers deposit almost all of their energy in the front section. Clusters due to obliquely incident particles tend to get split into two clusters, one cluster having all of its energy in the front submodule and one having all of its energy in the rear submodule. Therefore, clusters with less than half of their energy in the front section are discarded.

Several cuts reject photons whose energy is poorly measured. Clusters with fewer than 25 cells (corresponding to about 150 MeV energy deposit) are rejected,

as the energy resolution of low energy clusters is poor and the probability that they are fake is large. Showers near the edge of a calorimeter module are rejected, as they may have significant energy leakage out of the side of the module, and this leakage is not properly simulated in the energy calibration. Similarly, showers in sections of the Hex that are occluded by the PTC are discarded.

Pattern recognition fakes are purged with three cuts. A cluster is discarded if its position is poorly measured, that is, if the three projections that define its position do not intersect within 3 cm of a single point. Fake combinations frequently have a large discrepancy between the charge measured in each view, so any cluster with a view to view discrepancy over 40% is rejected. Another signature of a fake combination is excessive transverse shower width, so any cluster with transverse width larger than an energy dependent maximum (typically 50 mr) is also rejected.

A photon is eliminated as an electron bremsstrahlung if it is within 1.2° polar angle of a charged track whose dE/dx is consistent with the electron hypothesis ($\chi^2_{electron} < 2.0$). Interactions in the coil occasionally split a shower spatially, so neutral clusters within 40 mr (measured from the interaction point) are merged and a new energy is calculated.

4.2 TPC Photons

About 20% of the photons produced at the interaction point convert into an electron positron pair in the 0.2 radiation lengths of material between the interaction point and the TPC volume. Approximately 50% of the resulting charged particle pairs are identified as photons and the initial photon momentum is measured using geometrical reconstruction in the TPC.

Pairs of oppositely charged tracks that extrapolate to a common point separated from the interaction point are selected as conversion pair candidates. All charged tracks in this sample must have dE/dx consistent with the electron hypothesis, and the pair must have an invariant mass less than 60 MeV/c^2 (assuming electron masses). The opening angle must be less than a momentum dependent maximum, and the reconstructed momentum vector must point back toward the interaction point. Candidates that pass these cuts are joined with the photons measured by the Hex to form the final photon sample.

4.3 Monte Carlo

Monte Carlo simulations of the Hex and the TPC are necessary to understand how well photons and charged tracks are measured. This analysis requires a detailed understanding of the Hex performance, particularly pattern recognition efficiency and fake photon rate, so a detailed simulation of the Hex is necessary to study its performance. The TPC is not as vital to this analysis, so its Monte Carlo simulation is correspondingly less intricate, but still describes the data well.

For more information on the TPC detector simulation, see Marjory Shapiro's doctoral dissertation [33, p. 43].

The e^+e^- interactions in this Monte Carlo are simulated with different event generators depending on the particles produced. Purely QED interactions, such as Bhabha, $e^+e^- \rightarrow \tau^+\tau^-$, and $e^+e^- \rightarrow \mu^+\mu^-$ events are simulated by the Berends and Kleiss [34] Monte Carlo, which includes a simulation of initial and final state radiation, while multi-hadron events are simulated with the LUND event generator [35].

It is impossible to parameterize the output of the pattern recognition algorithm in the Hex. The pattern recognition algorithm does a simultaneous fit to all clusters in a module, so the location, size, and even the shape of each cluster effects the pattern reconstruction efficiency and the likelihood that fake photons are produced. Therefore, the input to, rather than the output of, the Hex pattern recognition is simulated. The Monte Carlo produces data that simulates the signal in the Hex electronics, then subjects this simulated data to the same pattern recognition and energy assignment routines used for real data. Therefore, the Monte Carlo simulation of the Hex reproduces the intricate dependencies on event topology found in real data.

The Monte Carlo simulation of the Hex is comprised of two main parts, the generation of showers and the simulation of the response of the Hex to these showers. Electromagnetic showers in the magnet coil and the calorimeter are simulated using EGS [32], while hadronic showers are simulated using a hadron shower Monte Carlo developed at CERN [36]. All material inside the calorimeter is included in the shower simulation, with the exception of the support rods, sense wires, nylon filaments, and material supporting the sense wire planes. The material between the TPC and the Hex is also simulated, although the internal structure of the magnet coil is ignored and a uniform, average density is used.

The Monte Carlo must be tuned carefully to properly simulate the response of an individual Geiger cell to a charged track. A Geiger discharge is simpler to simulate than a proportional mode discharge, since the Geiger discharge liberates a constant amount of charge when a cell fires. However, the conditions necessary to start a Geiger discharge (initial ionization, proximity to the sense wire or nylon filament, etc.) are difficult to predict and must be tuned empirically. The single cell simulation is tuned with data from cosmic rays incident on either an entire module or a single layer. Overall single cell efficiency and the path length dependence of this efficiency are checked with the average number of cells firing versus dip angle (Figure 4.3(a)), while the effect of the support rods (the regions at 7° and 16°) is tuned with the plot of average number of cells firing versus azimuth (Figure 4.3(b)). In this figure, particles are assumed to emanate from the beam interaction point, so angles are defined with respect to planes that pass through the origin of the PEP-4 detector system and are perpendicular to the front surface of the Hex module that detects the cluster. Dip angle is defined as the angle between a cluster and the plane normal to the beam line, while the azimuthal angle is defined as the angle between a cluster and the plane parallel to the longest side of the module. Both plots show the excellent agreement between

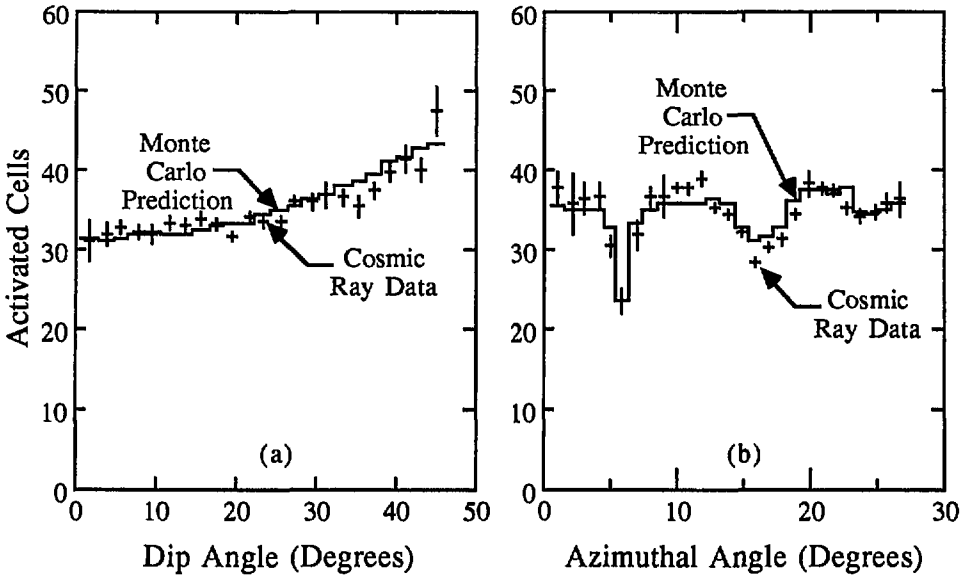

Figure 4.3: Activated Cells vs. Dip and Azimuthal Angle

the cosmic ray data and the Monte Carlo simulation.

The simulation generates showers using a list of particles impinging on the calorimeter and accumulates a list of the cells that fire. After the shower simulation is finished, the discharged cells are mapped to the proper electronics channels, and the response of the Hex electronics is simulated using measured values for anode/cathode charge matching, gain variations, electronics noise, non-linear ADC conversion, zero suppression, and bad channels.

The Monte Carlo is checked by comparing its predictions to real data from electrons and π^0's. The Monte Carlo and the real data both obtain the same relation between number of cells firing and electron momentum measured in the TPC (Figure 4.4), and the π^0 peak generated by the Monte Carlo has the proper mass and a width consistent with the π^0 width measured in the $\tau^+\tau^-$ event sample.

The response of the TPC to charged tracks passing through it is simulated in less detail than the response of the Hex. The ionization rate of each particle is smeared using the measured dE/dx resolution, while finite momentum resolution is simulated by smearing individual pad points according to the measured pad spatial resolution and fitting helixes through these points. This method simulates isolated tracks well, but does not exactly mimic the response of the TPC pattern recognition to overlapping tracks. Therefore, the simulation of photons reconstructed by the TPC is not as good as the simulation of photons detected by the Hex.

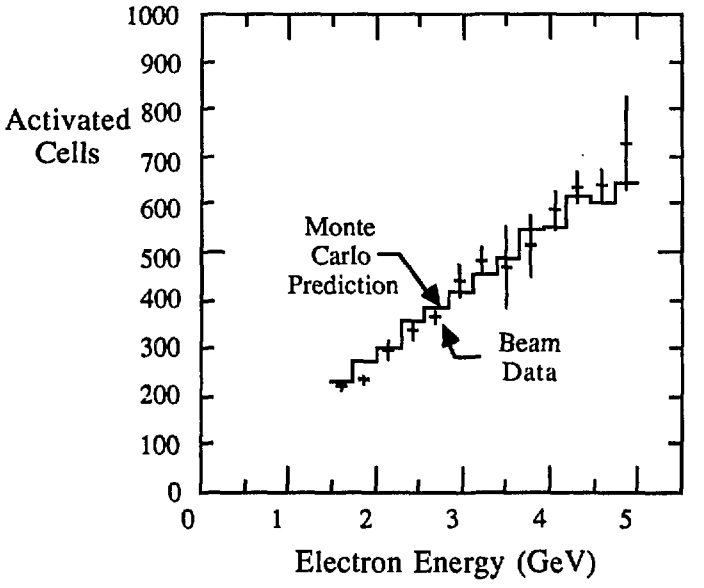

Figure 4.4: Cells vs. Electron Momentum

4.4 Performance

Each analysis step is associated with a measure of its performance. The measure of pattern recognition is efficiency – the probability that a produced photon is properly reconstructed. Energy resolution is the measure of how closely the reconstructed energy agrees with the actual energy. Purity, the measure of photon selection, is the probability that a reconstructed cluster is caused by an incident photon.

The Monte Carlo simulation is necessary to measure performance, since the correct position and energy is needed to calculate each quantity. The ability of the Monte Carlo to measure efficiency and energy resolution is checked with electrons, as the TPC can verify the measurements made by the Monte Carlo, and good agreement is found. Since the Monte Carlo reproduces electrons well, it should also provide reasonable estimates of photon performance.

Photons generated by the Monte Carlo must be linked to reconstructed photons to measure efficiency, energy resolution, or purity. It is impossible to link clusters by following a single photon through the Monte Carlo simulation since the Hex pattern recognition destroys all tagging information when it fits all photons within a module simultaneously. Therefore, a reconstructed photon is linked to a specific photon generated by the Monte Carlo if the reconstructed photon is found within 5 cm of the expected position and has a measured energy within 50% of the energy generated by the Monte Carlo.

Photon finding efficiency is the probability that a photon incident on the

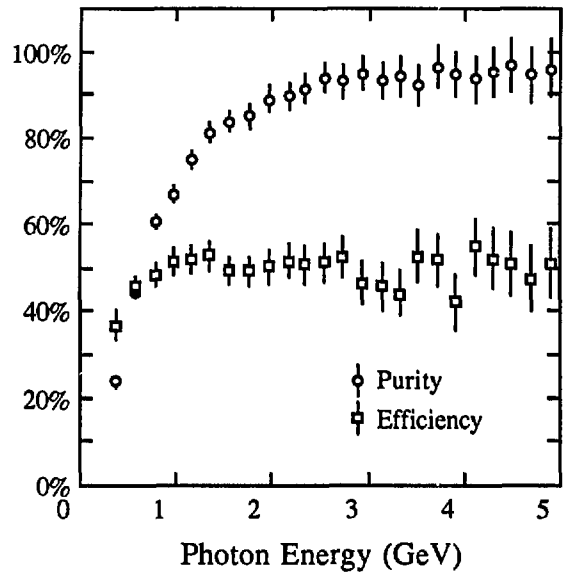

Figure 4.5: Hex Photon Finding Efficiency and Purity

Hex is properly reconstructed, where the definition of properly reconstructed is that the reconstructed cluster is linked to a photon in the Monte Carlo using the above algorithm. With this somewhat restrictive definition of efficiency, the photon finding efficiency for the $\tau^+\tau^-$ sample reaches a plateau around 50%, with a drop off below 1 GeV. The main cause of this low efficiency is accidental overlap with other particles. The initial $\tau^\pm$ is produced with an energy of 14.5 GeV, and the maximum p_T of any of its decay products is $m_\tau c/2 = 0.9$ GeV/c, so the final state particles in a $\tau^\pm$ decay tend to be collimated. Therefore, the shower from an individual photon is likely to be lost because it overlaps with the shower from another particle, resulting in a single shower. The energy dependence of the photon finding efficiency is plotted in Figure 4.5.

To measure the energy resolution, photons in $\tau^+\tau^-$ events produced by the Monte Carlo are linked with measured photons, and the difference between produced and measured energy is binned according to the produced energy. Each bin is fit with a Gaussian shape, and the resulting plot of energy resolution versus photon energy is plotted in Figure 4.6.

Purity, the probability that a measured cluster is produced by a real photon and is not an artifact of the pattern recognition algorithm, is measured by reversing the linking procedure. That is, we link Monte Carlo photons to reconstructed clusters rather than link reconstructed clusters to Monte Carlo photons. A Monte Carlo photon is linked to a reconstructed cluster if the Monte Carlo photon energy is within 50% of the reconstructed energy and the Monte Carlo photon extrapolates to a point within 5 cm of the reconstructed cluster. A re-

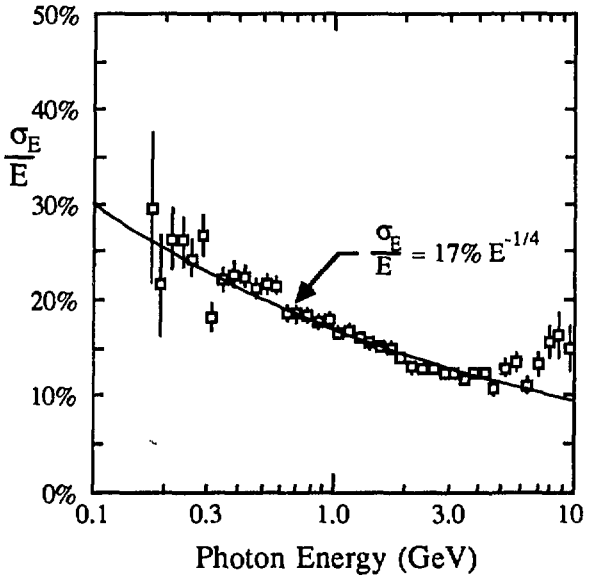

Figure 4.6: Hex Energy Resolution

constructed cluster is labeled as a true photon cluster if it has a Monte Carlo photon linked to it. The number of true photon clusters within an energy bin is divided by the total number of reconstructed clusters within that bin to find purity as a function of photon energy, plotted in Figure 4.5. For energies above 1 GeV, the photon sample is more that 80% pure.

Finally, the efficiency, purity, and energy resolution for photons reconstructed by the TPC are computed using algorithms similar to those used to measure the same quantities in the Hex. These measures of performance are significantly better at low energies for TPC photons than for Hex photons, but degrade significantly above a few GeV. Figures 4.7 and 4.8 show the TPC photon efficiency, purity, and energy resolution as functions of photon energy.

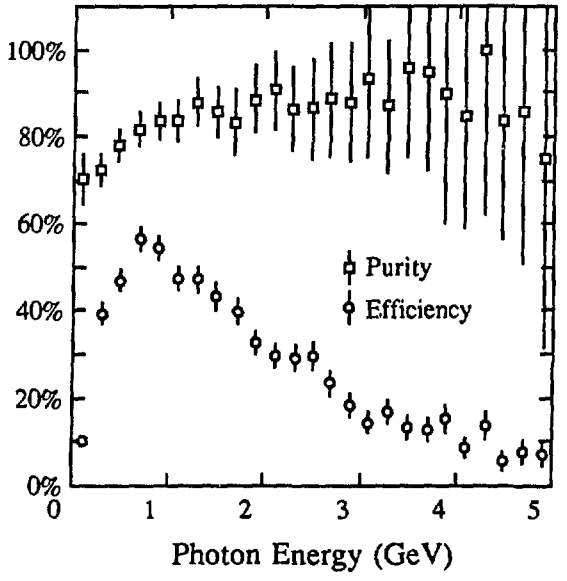

Figure 4.7: TPC Photon Finding Efficiency and Purity

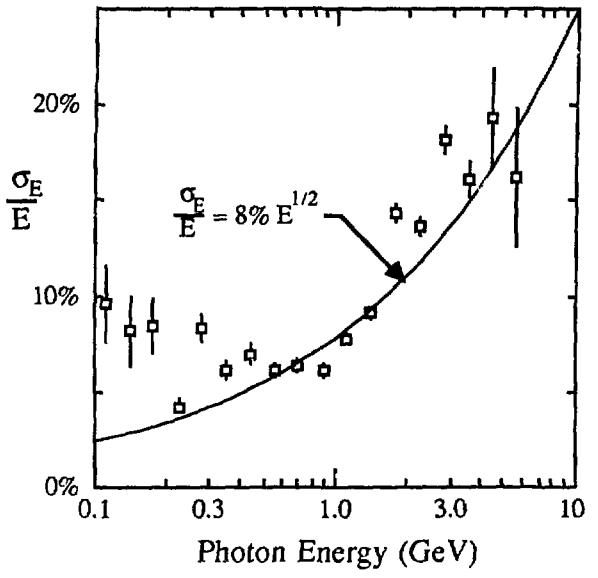

Figure 4.8: TPC Photon Energy Resolution

Chapter 5

Event Selection

This chapter describes the method used to select $\tau^+\tau^-$ events from the raw data sample. The selection is divided into two basic steps; the first step selects events mediated by a single virtual photon and the second step selects events in which the virtual photon turns into a $\tau^+\tau^-$ pair. Since the trigger is not 100% efficient, it does some inadvertent event selection, so the trigger efficiency is also discussed here.

5.1 One Photon Selection

Preanalysis attempts to select events due to e^+e^- interactions at the beam intersection point, such as $e^+e^- \rightarrow \gamma^* \rightarrow q\bar{q}$, $\mu^+\mu^-$, e^+e^-, or $\tau^+\tau^-$. However, many of the events accepted by preanalysis are not mediated by a single virtual photon, such as cosmic ray interactions, events with a beam particle interacting with a residual gas molecule, and events mediated by two virtual photons. Therefore, a software event selection is necessary to reject these background events. The one photon event selection is done exclusively with charged tracks measured by the TPC and is based solely on event topology – particle identification is not used at this point in the selection process.

The selection starts by identifying good tracks, where a good track is defined as a track with momentum greater than 150 MeV/c and, if the track momentum is less than 3.3 GeV/c, momentum error less than the momentum. In addition, the track must be more than 30° from the beam direction and the distance of closest approach to the nominal beam interaction point must be less than 10 cm in the Z direction and less than 5 cm in the XY plane.

Once good tracks have been identified, events with the desired topology are selected. Most cosmic ray and beam gas interactions are eliminated by rejecting events with less than two good tracks. Events mediated by two virtual photons are rejected by requiring the scalar sum of momentum transverse to the beam direction to be greater than 1.5 GeV/c and, in events with exactly two tracks, requiring one track to have more than 1.5 GeV/c transverse momentum.

5.2 Tau Selection

Further selection is necessary to obtain a nearly pure sample of $\tau^+\tau^-$ events from the output of the one photon event selection. Two distinct $\tau^+\tau^-$ samples are collected, one in which both $\tau^\pm$'s decay into one charged particle (τ_{1+1} sample) and one in which one $\tau^\pm$ decays into a single charged prong and the other $\tau^\pm$ decays into three charged particles (τ_{1+3} sample). Like the one photon event selection, the $\tau^+\tau^-$ event selection uses only charged track information from the TPC to reject background. Most of the selection is done with cuts on event topology, but particle identification is used to reject events at later stages.

The τ_{1+1} sample is most relevant here because this analysis measures exclusive decay modes of the $\tau^\pm$ involving a single charged particle, and about 85% of the one prong $\tau^\pm$ decays are contained in the τ_{1+1} sample. The τ_{1+3} sample is used only to estimate background levels. Therefore, the τ_{1+1} selection is described in more detail than the τ_{1+3} selection.

5.2.1 τ_{1+1} Selection

Events in which both $\tau^\pm$'s decay into a single charged particle (τ_{1+1} events) are characterized by two high momentum charged particles travelling in nearly opposite directions. The τ_{1+1} selection exploits this unusual event topology to obtain a sample that is approximately 90% pure.

The sources of background that must be eliminated are $q\bar{q}$, beam gas, $\mu^+\mu^-$, cosmic ray, Bhabha, and two-photon events. Beam gas and $q\bar{q}$ events are reduced by searching for events with exactly two charged tracks. Bhabha, $\mu^+\mu^-$, and cosmic ray events have two charged tracks, but these tracks are usually collinear, so the τ_{1+1} candidates are required to have two slightly acollinear tracks. Events mediated by two virtual photons frequently have two acollinear tracks, but the two tracks usually have a much smaller opening angle than τ_{1+1} events, so a maximum acollinearity is also required. The only significant source of background remaining after these cuts is radiative Bhabha events, so particle identification is used to require that at least one of the charged particles is not an electron.

The actual τ_{1+1} selection is as follows:

1. Tracks are categorized as *Conversion Electron*, *Good*, or *Hadron*.

   (a) *Conversion Electrons* are identified using the geometrical reconstruction algorithm described in TPC Photons (Section 4.2).

   (b) A *Good* track must meet the following criteria:

      i. The momentum is greater than 300 MeV/c.

      ii. If the momentum is less than 3.3 GeV/c, the momentum error is less than the momentum.

      iii. $\theta \geq 35°$, where θ is the angle between the particle momentum and the beam direction.

iv. dZ $\leq$ 5 cm, where dZ is the distance to the point of closest approach to the nominal interaction point in the Z direction.

v. dR $\leq$ 2 cm, where dR is the distance to the point of closest approach to the nominal interaction point in the XY plane.

vi. The track is not labeled as a *Conversion Electron.*

(c) In addition, single electrons or positrons resulting from photon conversions in which one particle is not reconstructed are labeled as *Conversion Electrons* if they pass the following cuts:

i. $\chi^2_{electron} < 9.0$, where $\chi^2_{electron}$ is the dE/dx chi-squared obtained assuming the electron hypothesis.

ii. $\chi^2_{hadron} > 9.0$, where χ^2_{hadron} is $\min(\chi^2_\pi, \chi^2_\mu, \chi^2_K, \chi^2_p)$.

iii. The track is not labeled as *Good.*

(d) *Hadrons* (which also include muons) are tracks that satisfy the following conditions:

i. $\chi^2_{hadron} < 7.0$.

ii. $\chi^2_{electron} > \chi^2_{hadron} + 3.0$.

iii. The track is labeled as *Good.*

iv. The track is not labeled as a *Conversion Electron.*

2. The two acollinear track topology is selected by requiring events to pass the following cuts:

(a) There is exactly one pair of *Good* tracks with acollinearity between 3° and 55°.

(b) The acollinear pair has acoplanarity between 1° and 55°, where the beam direction is the third direction used in the acoplanarity calculation.

(c) The two tracks in the acollinear pair have opposite charge.

(d) The event sphericity is less than 0.06 .

(e) The total number of reconstructed tracks is between 2 and 8.

(f) All tracks other than the acollinear pair are labeled as *Conversion Electrons.*

3. Beam gas and two-photon events are suppressed with the cuts:

(a) The scalar sum of the charged track momentum is $\geq$ 7.25 GeV/c.

(b) The scalar sum of the charged track momentum in each of the event hemispheres is greater than 0.65 GeV/c.

4. Bhabha and radiative Bhabha events are rejected by requiring:

(a) The scalar sum of the charged track momentum is $\leq$ 22 GeV/c.

(b) At least one of the tracks in the acollinear pair is labeled as a *Hadron*.

(c) If only one track is labeled as a *Hadron*, its momentum must be $\leq$ 9.5 GeV/c.

5. Background events that pass the above cuts because they have several badly measured tracks are rejected by loosening the cuts defining *Good* and *acollinear*, then requiring that the events pass the same selection.

The τ_{1+1} selection results in a sample of 1299 events, of which 116 are estimated to be background. The main sources of background, as determined by Monte Carlo simulation, are radiative Bhabha, τ_{1+3}, and two-photon events, in roughly equal amounts.

5.2.2 τ_{1+1} Selection Efficiency

The τ_{1+1} event selection must use dE/dx information to reject radiative Bhabha events, so the event selection efficiency depends on the species of the two charged particles in the final state. Almost all events in which both $\tau^{\pm}$'s decay into electrons are rejected, and events with one electron and one hadron have a lower selection efficiency than events with two charged hadrons. Selection efficiency also depends on the neutral particles in the event. The charged particle momentum spectrum is lower and angular distribution wider in decays that include neutral particles such as π^0's, so the topological cuts accept a slightly different fraction of these events. The dependence of the selection efficiency on the final state is determined by the Monte Carlo, and the results listed in Table 5.1. Note that measurements involving η's are efficiencies for the purely neutral η decay modes.

5.2.3 τ_{1+1} Trigger Efficiency

The TPC trigger, described in detail in Section 3.4, is divided into three general categories: charged trigger, neutral trigger, and mixed charged and neutral trigger. Each category has a different trigger criterion and none of the triggers is completely efficient, so the overall trigger efficiency for a particular τ_{1+1} event depends on the decay modes of the two $\tau^{\pm}$'s in the event. In particular, the overall efficiency is sensitive to the amount of electromagnetic energy (electrons, positrons, and photons) impinging on the Hex. To measure the trigger efficiencies for each decay type, we must first measure the individual trigger efficiencies and the correlations between them, then determine which triggers are relevant to a particular event. The data sample is divided into two samples, Experiment 11 and Experiment 12, that correspond to two slightly different trigger conditions, so the efficiency is measured separately for each experiment.

The efficiency of each trigger type is measured by selecting events in which another trigger is satisfied, then measuring the probability that the trigger in question is also satisfied. The efficiencies of the charged and neutral triggers are

τ^+ Decay	τ^- Decay	Efficiency(%)	Error(%)
$e^+\nu_e\overline{\nu}_\tau$	$e^-\overline{\nu}_e\nu_\tau$	0.7	0.1
$e^+\nu_e\overline{\nu}_\tau$	$\mu^-\overline{\nu}_\mu\nu_\tau, \pi^-\nu_\tau$	14.9	0.4
$e^+\nu_e\overline{\nu}_\tau$	$\rho^-\nu_\tau$	17.1	0.6
$e^+\nu_e\overline{\nu}_\tau$	$\pi^-\pi^0 X\nu_\tau$	17.0	0.6
$\mu^+\nu_\mu\overline{\nu}_\tau, \pi^+\overline{\nu}_\tau$	$\mu^-\overline{\nu}_\mu\nu_\tau, \pi^-\nu_\tau$	27.0	0.4
$\mu^+\nu_\mu\overline{\nu}_\tau, \pi^+\overline{\nu}_\tau$	$\rho^-\nu_\tau$	24.2	0.4
$\mu^+\nu_\mu\overline{\nu}_\tau, \pi^+\overline{\nu}_\tau$	$\pi^-\pi^0\pi^0\nu_\tau$	22.3	0.4
$\mu^+\nu_\mu\overline{\nu}_\tau, \pi^+\overline{\nu}_\tau$	$\pi^-\pi^0\pi^0\pi^0\nu_\tau$	20.7	0.4
$\mu^+\nu_\mu\overline{\nu}_\tau, \pi^+\overline{\nu}_\tau$	$\pi^-\pi^0\eta\nu_\tau$	18.9	0.4
$\rho^+\overline{\nu}_\tau$	$\rho^-\nu_\tau$	20.7	0.4
$\rho^+\overline{\nu}_\tau$	$\pi^-\pi^0\pi^0\nu_\tau$	18.6	0.4
$\rho^+\overline{\nu}_\tau$	$\pi^-\pi^0\pi^0\pi^0\nu_\tau$	18.3	0.4
$\rho^+\overline{\nu}_\tau$	$\pi^-\pi^0\eta\nu_\tau$	11.9	0.3
$\pi^+\pi^0\pi^0\overline{\nu}_\tau$	$\pi^-\pi^0\pi^0\nu_\tau$	15.9	0.3
$\pi^+\pi^0\pi^0\pi^0\overline{\nu}_\tau$	$\pi^-\pi^0\pi^0\pi^0\nu_\tau$	13.8	0.3
$\pi^+\pi^0\eta\overline{\nu}_\tau$	$\pi^-\pi^0\eta\nu_\tau$	11.3	0.3

Table 5.1: τ_{1+1} Event Selection Efficiency

accurately measured with this method, as they are completely independent, but the mixed charged and neutral trigger efficiency cannot be measured this way, as it is correlated with both the charged and the neutral triggers. Therefore, the mixed trigger efficiency is determined by measuring the efficiencies for the individual logical components of the trigger, then finding the probability that a trigger occurs if all of its logical components are satisfied.

The neutral trigger is sensitive only to energy in the Hex, so its efficiency is measured using both the τ_{1+3} and $q\overline{q}$ data samples. An efficiency of 91% in Experiment 11 and 98% in Experiment 12 is measured in each sample for events with more than 4 GeV of electromagnetic energy in the Hex. The main cause of the neutral trigger inefficiency is random electronic noise that causes the pretrigger signal to be out of time with the beam synchronization signal.

The charged trigger is most sensitive to the number of charged tracks, so its efficiency is measured with events that typically have two tracks – τ_{1+1} events and Bhabha events. The efficiency is 85% when measured with the entire τ_{1+1} sample, and is 85% for Experiment 11 and 90% for experiment 12 when measured with the Bhabha sample. Because of the difference between the measurements from the $\tau^+\tau^-$ and Bhabha data samples, a systematic error of 5% is assigned to this measurement. There are two main reasons for the charged trigger efficiency: random pretrigger inefficiency and a ripple being missed when a track is near the edge of a sector.

The mixed trigger efficiency for events with over 750 MeV of electromagnetic

energy in the Hex is 88% in Experiment 11 and 98% in Experiment 12. This efficiency is found by measuring the individual efficiencies of each logical component in this trigger, as well as the correlations between components, then using these measurements to compute the overall trigger efficiency. The major source of inefficiency is a hardware problem that results in zero efficiency for a portion of Experiment 11.

To measure the trigger efficiency as a function of decay type, decays are categorized by the amount of electromagnetic energy in the event, the amount of energy corresponding to the trigger thresholds for the neutral and the mixed charged and neutral triggers. Decays with less than 750 MeV electromagnetic energy are said to have *zero* electromagnetic energy, decays with between 750 MeV and 4 GeV have *small* electromagnetic energy, while events with greater than 4 GeV have *large* electromagnetic energy. An efficiency is assigned to each category, based on the efficiencies of the triggers that are relevant to this event.

Events with *zero* electromagnetic energy can only be triggered by the charged trigger, therefore the *zero* trigger efficiency is the same as the charged trigger efficiency, which is $(87 \pm 5)\%$ for both Experiment 11 and Experiment 12. Events with *large* electromagnetic energy can be triggered by both the neutral and the charged triggers, which are independent, so the *large* inefficiency is the product of the neutral inefficiency and the charged inefficiency. Therefore, the *large* trigger efficiency is 99% for Experiment 11 and 100% for experiment 12. Events with *small* electromagnetic energy are triggered primarily by the mixed charged and neutral trigger, but can also be triggered by the charged trigger. When the correlation between the mixed trigger and the charged trigger is taken into account, the efficiency for *small* trigger efficiency is 95% for Experiment 11 and 99% for experiment 12.

These results are summarized in Table 5.2. This classification scheme is rather crude, as some of the electromagnetic energy may not appear in the Hex and many of the decays labeled as having *small* electromagnetic energy frequently will have more than 4 GeV of electromagnetic energy, but the corrections based on these efficiencies are both small and insensitive to flaws in the classification scheme.

5.3 τ_{1+3} Selection

Events in which one $\tau^{\pm}$ decays into a single charged particle and the other $\tau^{\mp}$ decays into three charged prongs (τ_{1+3} events) are characterized by a single, high momentum charged track opposite to three charged tracks. This event topology is exploited by the τ_{1+3} selection to obtain a sample that is approximately 95% pure. Like the τ_{1+1} selection, the sources of background that must be eliminated are $q\bar{q}$, beam gas, $\mu^+\mu^-$, cosmic ray, Bhabha, and two-photon events.

The τ_{1+3} selection is as follows:

1. Tracks are categorized as *Conversion Electron* or *Good.*

τ^+ Decay Mode	τ^- Decay Mode	Experiment 11 Efficiency(%)	Experiment 12 Efficiency(%)
$\mu^+\nu_\mu\overline{\nu}_\tau, \pi^+\overline{\nu}_\tau$	$\mu^-\overline{\nu}_\mu\nu_\tau, \pi^-\nu_\tau$	87	87
$\mu^+\nu_\mu\overline{\nu}_\tau, \pi^+\overline{\nu}_\tau$	$\rho^-\nu_\tau$	95	99
$\mu^+\nu_\mu\overline{\nu}_\tau, \pi^+\overline{\nu}_\tau$	$\pi^-\pi^0 X\nu_\tau$	95	99
$\rho^+\overline{\nu}_\tau$	$\rho^-\nu_\tau$	95	99
$\rho^+\overline{\nu}_\tau$	$\pi^-\pi^0 X\nu_\tau$	95	99
$\pi^+\pi^0 X\overline{\nu}_\tau$	$\pi^-\pi^0 X\nu_\tau$	95	99
$e^+\nu_e\overline{\nu}_\tau$	$e^-\overline{\nu}_e\nu_\tau$	99	100
$e^+\nu_e\overline{\nu}_\tau$	$\mu^-\overline{\nu}_\mu\nu_\tau, \pi^-\nu_\tau$	99	100
$e^+\nu_e\overline{\nu}_\tau$	$\rho^-\nu_\tau$	99	100
$e^+\nu_e\overline{\nu}_\tau$	$\pi^-\pi^0 X\nu_\tau$	99	100

Table 5.2: τ_{1+1} Trigger Efficiency

(a) *Conversion Electrons* are identified using the geometrical reconstruction algorithm described in TPC Photons (Section 4.2).

(b) A *Good* track must meet the following criteria:

i. The momentum is greater than 300 MeV/c.

ii. If the momentum is less than 3.3 GeV/c, the momentum error is less than the momentum.

iii. $\theta \geq 30°$, where θ is the angle between the particle momentum and the beam direction.

iv. dZ $\leq$ 10 cm, where dZ is the distance to the point of closest approach to the nominal interaction point in the Z direction.

v. dR $\leq$ 5 cm, where dR is the distance to the point of closest approach to the nominal interaction point in the XY plane.

vi. The track is not labeled as a *Conversion Electron*.

2. Events with a 1+3 topology are selected by requiring events to pass the following cuts:

(a) There are exactly four *Good* tracks, with zero total charge.

(b) There is exactly one isolated *Good* track that makes an angle $\geq 140°$ with each of the other three *Good* tracks.

(c) The total number of reconstructed tracks is less than 10.

(d) All tracks other than the four *Good* tracks are labeled as *Conversion Electrons*.

3. Beam gas and two-photon events are suppressed with the following cuts:

(a) The scalar sum of the charged track momentum is $\geq$ 4.5 GeV/c.

(b) The invariant mass of the four *Good* tracks is ≥ 3 GeV/c^2 (assuming pion masses).

(c) The invariant mass of the three *Good* tracks (ie. without the isolated track) is ≤ 2 GeV/c^2 (assuming pion masses).

4. Bhabha and radiative Bhabha events are rejected by requiring:

(a) The scalar sum of the charged track momentum is ≤ 24 GeV/c.

(b) The isolated *Good* track has acollinearity $\geq 2°$ with each of the other three *Good* tracks.

(c) None of the tracks on the three side is labeled as an *Electron*, where *Electrons* are tracks that satisfy the following conditions:

i. $\chi^2_{electron} < 9.0$.

ii. $\chi^2_{hadron} > 9.0$.

iii. The track is labeled as *Good*.

The τ_{1+3} selection results in a sample of 669 events, of which 41 are estimated to be background. The main sources of background, as determined by Monte Carlo simulation, are 20 ± 3 $q\bar{q}$ and 13 ± 4 τ_{1+1} events. The selection efficiency for τ_{1+3} events, again determined by the Monte Carlo simulation, is 22.7%.

Chapter 6

Measurement of the Rho Branching Fraction

Having described the methods used to select and reconstruct $\tau^+\tau^-$ events, the physics analysis of $\tau^\pm$ decays is begun with the measurement of the branching fraction for the decay mode $\tau^- \to \nu_\tau \rho^-$. The τ_{1+1} data sample is too small to improve the existing measurement of $B(\tau^- \to \nu_\tau \rho^-) = (22.1 \pm 1.4)\%$ [5,37], but our measurement of the $\tau^- \to \nu_\tau \rho^-$ branching fraction is used as a benchmark for checking our π^0 reconstruction efficiency.

6.1 Rho Reconstruction

This section describes the methods for reconstructing $\rho^\pm$'s. The $\rho^\pm$ decays essentially 100% of time into $\pi^\pm\pi^0$ [5], so we begin the $\rho^\pm$ reconstruction by identifying $\pi^\pm$'s and reconstructing π^0's, then observe $\rho^\pm$'s in the $\pi^\pm\pi^0$ invariant mass distribution. This invariant mass plot contains significant background, so a method for determining the number of combinations due to $\rho^\pm$ decay is also presented. The τ_{1+1} event sample (Section 5.2.1) is used to calculate the branching fraction $B(\tau^- \to \nu_\tau \rho^-)$, as 85% of the $\tau^- \to \nu_\tau \rho^-$ decays are contained in this sample.

6.1.1 Charged Pion Selection

The TPC selects $\pi^\pm$ candidates using the measured dE/dx energy loss and the particle momentum, as described in Section 3.2.3. Loose cuts maximize the $\rho^\pm$ acceptance, so all charged tracks with dE/dx ionization rate consistent with the $\pi^\pm$ hypothesis ($\chi^2_\pi \leq 9.0$) are accepted as $\pi^\pm$ candidates. The τ_{1+1} event selection must label this track as a primary $\tau^\pm$ decay product, so $\pi^\pm$ candidates must also pass the *Good* track criteria described in Section 5.2.1.

6.1.2 Neutral Pion Reconstruction

Nearly all π^0's decay into two photons [5], so π^0's are reconstructed by computing the invariant mass of all γ-γ combinations in the τ_{1+1} sample, then searching for

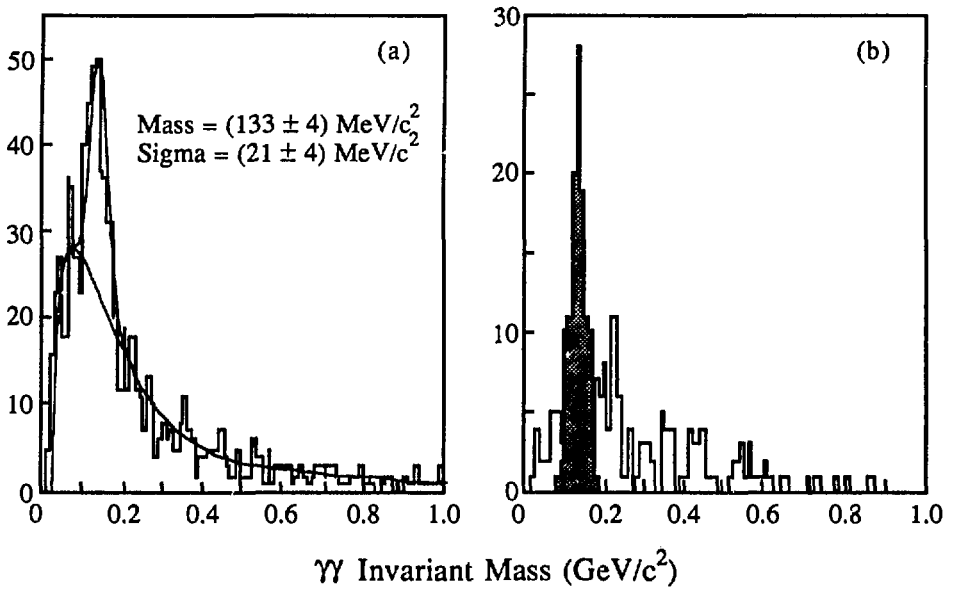

Figure 6.1: γ-γ Invariant Mass

an enhancement at the π^0 mass. The invariant mass distribution of all photons that pass the cuts described in Section 4.1.3 is plotted in Figure 6.1(a). A clear enhancement is seen near the π^0 mass (135 MeV/c^2), along with a large amount of background. The amount of background in the γ-γ invariant mass distribution shown in this figure can be dramatically reduced by applying kinematical cuts to the γ-γ combinations. Figure 6.1(b) shows the invariant mass of all γ-γ combinations that have $P_{\gamma\gamma} \geq 1.5$ GeV/c and a center of mass decay angle $\cos\theta_{cm} \leq 0.6$. The background is strongly suppressed, although the size of the π^0 signal is also reduced.

The above method demonstrates that a π^0 signal is seen when the entire τ_{1+1} sample is combined, but does not identify individual π^0's. To select individual π^0 candidates, the measured photon energies and positions are combined with the photon energy resolution plotted in Figure 4.6 and a one-constraint fit is made to the π^0 mass. A γ-γ combination is accepted as a π^0 candidate if the fit yields $\chi^2_{\pi^0} \leq 4.0$. When this method is applied to the γ-γ sample in Figure 6.1(b), the entries forming the shaded region are selected as π^0 candidates.

Different values for $P_{\gamma\gamma}$ and $\cos\theta_{cm}$ are used to select π^0 candidates, depending on the requirements of the analysis. Tight cuts (larger values for $P_{\gamma\gamma}$ and smaller values for $\cos\theta_{cm}$) increase the signal to noise ratio, but decrease the total amount of signal. Conversely, loose cuts increase the amount of signal observed but increase the background contamination in that signal. The $\rho^{\pm}$ analysis requires small background, as the major systematic error is due to background subtraction, yet needs enough signal to be statistically significant. Therefore, a

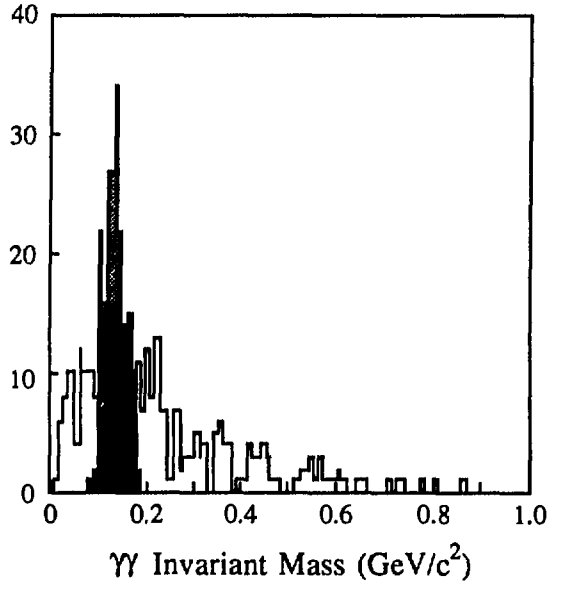

Figure 6.2: γ-γ Invariant Mass

compromise is struck between maximal acceptance and minimal background and the cuts for the $\rho^{\pm}$ reconstruction are set at $P_{\gamma\gamma} \geq 1.0$ GeV/c and $\cos\theta_{cm} \leq 0.6$. The γ-γ invariant mass distribution obtained with these cuts is shown in Figure 6.2, along with those combinations selected as π^0 candidates (shaded region).

6.1.3 Rho Reconstruction

Charged ρ's are identified by calculating the invariant mass of the $\pi^{\pm}\pi^0$ system, where the $\pi^{\pm}$ selection and the π^0 reconstruction are described above. To insure that both π's are from the same $\tau^{\pm}$, the $\pi^{\pm}$ and the π^0 are required to be in the same event hemisphere, and background due to hadronic interactions in the Hex is reduced by requiring a minimum open angle (lab frame) between the two π's. Figure 6.3 shows the invariant mass distribution of all $\pi^{\pm}\pi^0$ combinations with lab frame opening angle ($0.5 \leq \cos\theta_{lab} \leq 0.99$). A clear peak is seen near the ρ mass (776 MeV/c^2).

The number of $\rho^{\pm}$'s in the peak is measured using the following method. First, the shape of the $\pi^{\pm}\pi^0$ invariant mass distribution expected from $\rho^{\pm}$ decays is obtained by generating $\tau^- \rightarrow \nu_\tau\rho^- \rightarrow \nu_\tau\pi^-\pi^0$ decays with the Monte Carlo, then requiring the Monte Carlo events to pass the same τ_{1+1} event selection described in Section 5.2.1. The $\pi^{\pm}$ and π^0 candidates are selected with the algorithms described in Sections 6.1.1 and 6.1.2, and the $\pi^{\pm}\pi^0$ invariant mass distribution is computed for all combinations that satisfy the angular cuts described in the

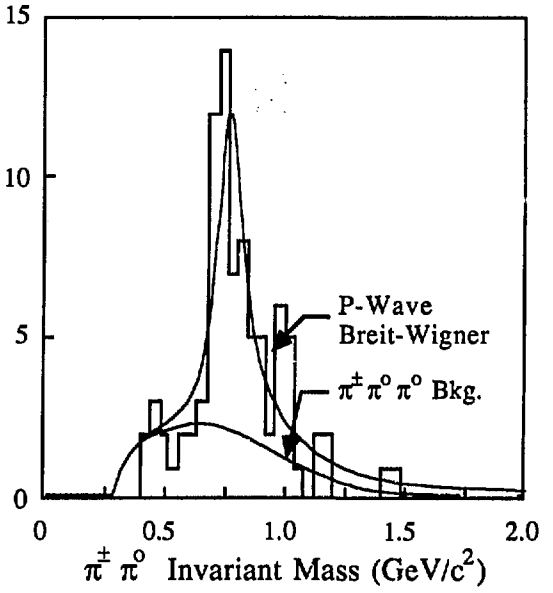

Figure 6.3: $\pi^{\pm}\pi^0$ Invariant Mass

previous paragraph. The resulting invariant mass distribution (Figure 6.4(a)) is fit to a P-Wave Breit-Wigner shape [38] with the Area, Mass, and Width as free variables. The best fit is obtained with $m = (765 \pm 7)$ MeV/c^2 and $\Gamma = (135 \pm 15)$ MeV/c^2, which is consistent with the world average of $m_\rho = 776$ MeV/c^2 and $\Gamma_\rho = 155$ MeV/c^2 [5]. Next, the shape of the background is obtained in an analogous way, except that the decay mode generated by the Monte Carlo is $\tau^- \rightarrow \nu_\tau \pi^- \pi^0 \pi^0$ (non-resonant) and the function used to fit the distribution simulates phase space [39] rather than a Breit-Wigner distribution (Figure 6.4(b)). Finally, the number of $\rho^{\pm}$'s observed in the τ_{1+1} data sample is obtained by fitting the observed $\pi^{\pm}\pi^0$ invariant mass distribution to the sum of $\rho^{\pm}$ signal and $\pi^{\pm}\pi^0\pi^0$ background, with the signal and background shapes fixed to the shapes predicted by the Monte Carlo and the amplitudes allowed to vary. The best fit, shown in Figure 6.3, measures 52.5 entries in the $\rho^{\pm}$ peak.

6.2 Branching Fraction Measurement

The number of reconstructed $\rho^{\pm}$'s must now be converted into a branching fraction. Although the branching fraction is just the number of $\rho^{\pm}$'s produced divided by the number of produced $\tau^{\pm}$'s, the actual computation is complicated because only a fraction of these $\tau^{\pm}$'s and $\rho^{\pm}$'s are correctly identified. This section describes the computation, then converts the 52.5 reconstructed $\rho^{\pm}$'s into the branching fraction for $\tau^- \rightarrow \nu_\tau \rho^-$.

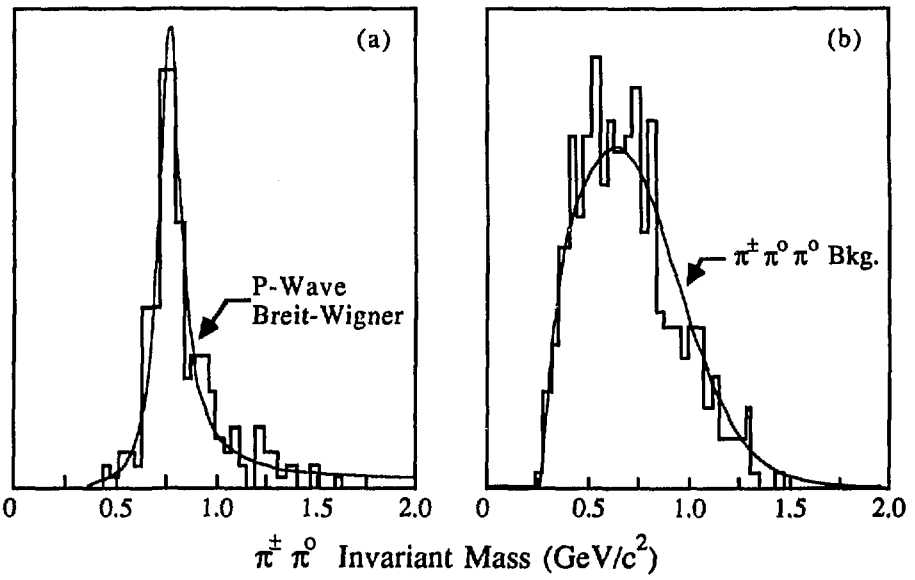

Figure 6.4: $\pi^{\pm}\pi^0$ Invariant Mass (Monte Carlo)

6.2.1 Measurement Method

Simply stated, the method used to convert the number of reconstructed $\rho^{\pm}$'s into a branching fraction is to compare the number of reconstructed $\rho^{\pm}$'s to the number of τ_{1+1} events. Although some additional details complicate the actual calculation, the basic principle is demonstrated by comparing the formula for the number of events in the τ_{1+1} sample to the formula for the number of reconstructed $\rho^{\pm}$'s.

For a given integrated e^+e^- luminosity ($\mathcal{L}_{e^+e^-}$) and cross section for e^+e^- into $\tau^+\tau^-$ ($\sigma_{\tau^+\tau^-}$), the number of events in the τ_{1+1} sample is given by

$$N_{\tau_{1+1}} = N_{\tau\tau} \cdot B_1 \cdot B_1 \cdot \epsilon_{trig} \cdot \epsilon_{select}, \tag{6.1}$$

where $N_{\tau\tau}$ ($= \mathcal{L}_{e^+e^-} \cdot \sigma_{\tau^+\tau^-}$) is the total number of $\tau^+\tau^-$ events produced, B_1 is the inclusive branching fraction of τ^- into one charged track (measured to be $(86.5 \pm 0.3)\%$ [5]), ϵ_{trig} is the trigger efficiency, and ϵ_{select} is the τ_{1+1} event selection efficiency. The number of $\rho^{\pm}$'s reconstructed is given by

$$\begin{aligned} N_\rho(\text{reconstructed}) &= 2 \cdot N_{\tau\tau} \cdot (B_1 - B_\rho) \cdot B_\rho \cdot \epsilon_{trig} \cdot \epsilon_{select} \cdot \epsilon^1_{recon} \\ &\quad + N_{\tau\tau} \cdot B_\rho \cdot B_\rho \cdot \epsilon_{trig} \cdot \epsilon_{select} \cdot \epsilon^2_{recon}, \end{aligned} \tag{6.2}$$

where B_ρ is the branching fraction for the decay mode $\tau^- \rightarrow \nu_\tau \rho^-$ and ϵ^n_{recon} is the average number of $\rho^{\pm}$'s reconstructed when n $\rho^{\pm}$'s are produced in an event (the allowed range for ϵ^n_{recon} is from 0 to n).

All of the variables in Equations 6.1 and 6.2, with the exception of $N_{\tau\tau}$ and B_ρ, can either be measured with data or predicted by Monte Carlo simulation. Therefore, Equation 6.1 is solved for $N_{\tau\tau}$, and this value is inserted into Equation 6.2, which is then solved for B_ρ. Notice that this method uses the measured inclusive one prong branching fraction B_1 to determine the number of $\tau^+\tau^-$ events rather than computing $N_{\tau\tau}$ from the product of the integrated e^+e^- luminosity and the $\tau^+\tau^-$ cross section. This is because the error in the measurement of $\mathcal{L}_{e^+e^-}$ is approximately 7%, so computing $N_{\tau\tau}$ with $\mathcal{L}_{e^+e^-}$ adds an additional 7% systematic error to the $\tau^- \to \nu_\tau\rho^-$ branching fraction measurement.

The actual calculation is more complicated because ϵ_{trig} and ϵ_{select} depend on the decay mode, while ϵ_{trig} and ϵ^n_{recon} depend on the experimental period. To properly compute the $\tau^- \to \nu_\tau\rho^-$ branching fraction, Equation 6.1 must be re-written as

$$N_{\tau_{1+1}} = \sum_{exp} N_{\tau\tau}(exp) \cdot \sum_x \sum_y B_x \cdot B_y \cdot \epsilon_{trig}(exp, x, y) \cdot \epsilon_{select}(x, y), \qquad (6.3)$$

where x and y are the possible $\tau^\pm$ one prong decay modes ($\sum_x B_x = B_1$). Similarly, Equation 6.2 is re-written as

$$\begin{aligned} N_\rho(\text{reconstructed}) \;=\; & 2 \cdot \sum_{exp} N_{\tau\tau}(exp) \cdot \sum_{x \neq \rho} B_x \cdot B_\rho \cdot \\ & \epsilon_{trig}(exp, x, \rho) \cdot \epsilon_{select}(x, \rho) \cdot \epsilon^1_{recon}(exp) \\ & + \sum_{exp} N_{\tau\tau}(exp) \cdot B_\rho \cdot B_\rho \cdot \epsilon_{trig}(exp, \rho, \rho) \cdot \\ & \epsilon_{select}(\rho, \rho) \cdot [\epsilon^2_{recon}(exp) - 2\epsilon^1_{recon}(exp)]. \qquad (6.4) \end{aligned}$$

As before, all variables in Equations 6.3 and 6.4, with the exception of $N_{\tau\tau}(exp)$ and B_ρ, can either be measured with the beam data or predicted by the Monte Carlo. Therefore, these two equations can be solved simultaneously to obtain a measurement for B_ρ.

6.2.2 Computation Details

The computation of the branching fraction for $\tau^- \to \nu_\tau\rho^-$ is now reduced to obtaining the values for the variables in Equations 6.3 and 6.4. The data are divided into three experimental periods corresponding to the different trigger configurations (Section 5.2.3) and the number of functional Hex modules (Section 3.3.5). Table 6.1 summarizes the configuration in each of the three experimental periods.

The values for the selection efficiencies $\epsilon_{select}(x, y)$ are listed in Table 5.1. These values are predicted with the Monte Carlo simulation as described in Section 5.2.1 and are between 15% and 25%, except for $\epsilon_{select}(e^+, e^-)$ which is $< 1\%$. Similarly, values for the trigger efficiencies $\epsilon_{trig}(exp, x, y)$ are listed in Table 5.2. These efficiencies are measured with beam data as described in Section 5.2.3 and

Experimental Period	Trigger Configuration	Number of Active Hex Modules	Measured $\mathcal{L}_{e^+e^-}$ (pb^{-1})
I	Exp. 11	5	30.9
II	Exp. 12	5	13.8
III	Exp. 12	4	26.5

Table 6.1: Experimental Configuration

Decay Mode	Branching Fraction (%)
$\tau^- \rightarrow \nu_\tau e^- \overline{\nu}_e$	18.9
$\tau^- \rightarrow \nu_\tau \mu^- \overline{\nu}_\mu$	18.4
$\tau^- \rightarrow \nu_\tau \pi^-$	11.5
$\tau^- \rightarrow \nu_\tau \rho^-$	24.0
$\tau^- \rightarrow \nu_\tau K^{*-}$	2.6
$\tau^- \rightarrow \nu_\tau A^-(1270)$	14.2
$\tau^- \rightarrow \nu_\tau \rho^-(1600)$	10.4
$\rho(1600) \rightarrow A(1270)\pi$	57.8
$\rho(1600) \rightarrow \pi\pi\pi\pi$	14.6
$\rho(1600) \rightarrow \pi\pi$	27.6
$A(1270) \rightarrow \rho\pi$	100

Table 6.2: Monte Carlo Generated Branching Fractions

are typically between 95% and 100%. The values for B_n are based on the Particle Data Book [5] values, but are adjusted slightly to sum to 100%. These values, listed in Table 6.2, are used to make small corrections to the trigger and event selection efficiencies, corrections that are insensitive to the values used for B_n.

The values for the reconstruction efficiencies $\epsilon^n_{recon}(exp)$ are determined by Monte Carlo simulation. We generate $\tau^+\tau^-$ events with the decay of each $\tau^\pm$ simulated according to the decay modes listed in Table 6.2. The number of reconstructed $\rho^\pm$'s is obtained using the fitting method described in Section 6.1, then divided by the number of generated $\rho^\pm$'s to obtain a crude measurement of the $\rho^\pm$ reconstruction efficiency. This crude measurement is corrected for the effect of inactive modules to obtain the values for $\epsilon^n_{recon}(exp)$ listed in Table 6.3.

We now have values for all variables in Equations 6.3 and 6.4. Equation 6.3 is combined with the ratio of the measured values of luminosity (Table 6.1) to obtain values for $N_{\tau\tau}(exp)$. Equation 6.4 is then solved for B_ρ, yielding $B_\rho = 31.1\%$. However, B_ρ is the *inclusive* branching fraction for the decay $\tau^- \rightarrow \nu_\tau \rho^- X$, not the *exclusive* branching fraction for the decay $\tau^- \rightarrow \nu_\tau \rho^-$. That is, B_ρ

Reconstruction Efficiency	5 Active Modules	4 Active Modules
ϵ^1_{recon}	6.2%	4.6%
ϵ^2_{recon}	12.6%	10.2%

Table 6.3: $\rho^{\pm}$ Reconstruction Efficiency

contains contributions from the feed down decays $\tau^- \rightarrow \nu_\tau A^-(1270) \rightarrow \nu_\tau \rho^- \pi^0$ and $\tau^- \rightarrow \nu_\tau \rho^-(1600) \rightarrow \nu_\tau \rho^- \pi^0 \pi^0$. The inclusive branching fraction is converted to an exclusive branching fraction by subtracting the predicted contribution from these feed down decays, yielding an exclusive branching fraction

$$B(\tau^- \rightarrow \nu_\tau \rho^-) = (22.6 \pm 3.1)\%, \tag{6.5}$$

where the error quoted only includes the statistical error.

6.2.3 Systematic Errors

All variables in Equations 6.3 and 6.4 have measurement errors associated with them, errors that lead to systematic errors in the measurement of the $\tau^- \rightarrow \nu_\tau \rho^-$ branching fraction. The amount that each measurement error contributes to the total systematic error is calculated by observing the change made in the branching fraction measurement when each input variable is varied by its error. Since these systematic errors are proportional to the $\tau^- \rightarrow \nu_\tau \rho^-$ branching fraction, all systematic errors are quoted as a percentage of the branching fraction.

The major source of systematic error is the uncertainty in the background to the $\rho^{\pm}$ signal. The decay modes involving more than one neutral meson have not been measured precisely [6], so the background shape in the $\pi^{\pm}\pi^0$ invariant mass distribution (Figure 6.4(b)) is uncertain, as is the feed down subtraction used to convert the inclusive branching fraction into an exclusive branching fraction.

The systematic error due to uncertainty in the feed down subtraction is obtained by varying the branching fractions of the decay modes that contribute to feed down. The values for the branching fractions of feed down decays are based on the measured $\tau^- \rightarrow \nu_\tau \pi^- \pi^- \pi^+ (+neutrals)$ branching fractions [2,21], but the quoted errors for the $3\pi^{\pm}$ branching fractions are multiplied by approximately 2.5 in order to reflect the uncertainty in their relation to the $\tau^- \rightarrow \nu_\tau \pi^- \pi^0 \pi^0 (+neutrals)$ branching fractions. Therefore, the branching fractions for feed down decay modes are varied by 25% of their nominal values, which changes the value for the $\tau^- \rightarrow \nu_\tau \rho^-$ branching fraction by 10.6% of its value.

The systematic error due to the invariant mass background shape is estimated by generating Monte Carlo events with a different background shape. Events are generated with the τ^- branching fractions listed in Table 6.2, except the branching fraction of the $A(1270)$, which is changed to 50% $A(1270) \rightarrow \rho\pi$ and

Error Source	Error (%)
Feed Down	10.6
Background Shape	9.3
ϵ_{trig}	3.5
ϵ_{select}	3.3
B_π	2.2
Luminosity	0.7
B_1	0.6
Total	15.1

Table 6.4: Systematic Errors

50% $A(1270) \rightarrow \eta\pi\pi$. When the resulting $\pi^\pm\pi^0$ invariant mass distribution is fit to the $\rho^\pm$ plus non-resonant $\pi^\pm\pi^0\pi^0$ background, as in Section 6.1.3, the fraction of produced $\rho^\pm$'s decreases by an amount that leads to a systematic error due to uncertainty in the background shape of 9.3%.

The contributions to the systematic error from all other sources are small compared to the error due to the uncertainty in the background composition. Their contributions are estimated by changing each variable by 10% to 20% of its nominal value, then re-calculating the $\tau^- \rightarrow \nu_\tau\rho^-$ branching fraction. Table 6.4 lists all contributions to the systematic error quoted as a percentage of the branching fraction, which are added in quadrature to obtain the total systematic error.

6.2.4 Final Result

The final value for the branching fraction for the decay $\tau^- \rightarrow \nu_\tau\rho^-$ is obtained by including the systematic error into the branching fraction quoted in Equation 6.5. The result is

$$B(\tau^- \rightarrow \nu_\tau\rho^-) = (22.6 \pm 3.1 \pm 3.4)\%, \tag{6.6}$$

where the first error is the statistical error and the second error is the systematic error.

Chapter 7

Measurement of the Multiple Neutral Meson Branching Fraction

This chapter describes the main analysis of this thesis – the measurement of the inclusive branching fraction for $\tau^{\pm}$ decays that involve a single charged pion accompanied by more than one neutral meson, that is, the inclusive branching fraction $B(\tau^- \to \nu_\tau \pi^- \pi^0 + \mathrm{n}h^0)$, where $\mathrm{n} \geq 1$ and h^0 is a π^0 or an η.

7.1 Event Reconstruction

This section describes the method for identifying $\tau^{\pm}$ decays involving more than one neutral meson. It is difficult to completely reconstruct these decays because of low reconstruction efficiency ($\sim$ 5% per neutral meson) and combinatorial background, so the τ_{1+1} sample (Section 5.2.1) is searched for decays in which one π^0 is reconstructed and additional neutral energy is observed. As in the measurement of $B(\tau^- \to \nu_\tau \rho^-)$, only the τ_{1+1} event sample is used to calculate the branching fraction as 85% of the multiple neutral meson decays are contained in this sample. Since the additional neutral meson(s) is detected by observing energetic photons and not by explicit reconstruction, the detection efficiency is greatly improved but the distinction between modes is lost. As a result, the analysis is primarily sensitive to the sum of all branching fractions involving more than one neutral meson rather than the individual branching fractions.

The decay modes of the $\tau^{\pm}$ with more than one neutral meson that are predicted to have non-zero single prong branching fractions [1] are listed in Table 7.1. Each of these decay modes contains one π^0 and at least one additional neutral meson, so the analysis method outlined in the previous paragraph is sensitive to all multiple neutral meson decay modes that are expected to have significant branching fractions. Note that since only single charged particle final states are considered, all numbers quoted for branching fractions involving an η are:

$$B(\tau^- \to \nu_\tau \pi^- \pi^0 \eta) \cdot B(\eta \to \text{all neutrals}).$$

Decay Mode	Predicted Branching Fraction (%)
$\tau^- \rightarrow \nu_\tau \pi^- \pi^0 \pi^0$	7.1%
$\tau^- \rightarrow \nu_\tau \pi^- \pi^0 \pi^0 \pi^0$	1.0%
$\tau^- \rightarrow \nu_\tau \pi^- \pi^0 \eta$	0.5%

Table 7.1: Predicted Branching Fractions

Also note that while the decay modes quoted with upper limits in Table 2.4 are not included in Table 7.1, as no contribution is expected from any of these decay modes, this analysis method is still sensitive to these decay modes.

7.1.1 Charged Pion Selection

The TPC selects $\pi^\pm$ candidates by comparing the measured dE/dx energy loss with the particle momentum, as described in Section 3.2.3. Loose cuts maximize the multiple neutral meson sample and the background is expected to be small, so all charged tracks with dE/dx ionization rate consistent with the $\pi^\pm$ hypothesis ($\chi^2_\pi \leq 9.0$) are accepted as $\pi^\pm$ candidates. The τ_{1+1} event selection must label this track as a primary $\tau^\pm$ decay product, so $\pi^\pm$ candidates must also pass the *Good* track criteria described in Section 5.2.1.

7.1.2 Neutral Pion Reconstruction

All π^0 candidates in this analysis are reconstructed via their decay into two photons, where the photons are identified either by the Hex or the TPC as described in Section 4.1.3. Large π^0 acceptance is necessary, so the method described in Section 6.1.2, with loose cut values, is used to select π^0 candidates. Briefly stated, π^0 candidates are selected by calculating the invariant mass for all γ-γ combinations that have $P_{\gamma\gamma} \geq 1.0$ GeV/c and making a one constraint fit to the π^0 mass. If the fit yields $\chi^2_{\pi^0} \leq 4.0$, the γ-γ combination is accepted as a π^0 candidate. The γ-γ invariant mass distribution is shown in Figure 7.1, along with those combinations selected as π^0 candidates (shaded region).

7.1.3 Additional Neutral Energy Requirement

Once a π^0 candidate is found, the decay is searched for additional neutral energy that is presumed to come from the decays of π^0's or η's. If a non-trivial amount of additional neutral energy is observed in the same decay hemisphere as the π^0, the decay is considered a multiple neutral meson decay. Specifically, the energies of all photons in the same hemisphere as the reconstructed π^0 (excluding the two photons from the π^0) are summed, and the decay is counted as a multiple neutral

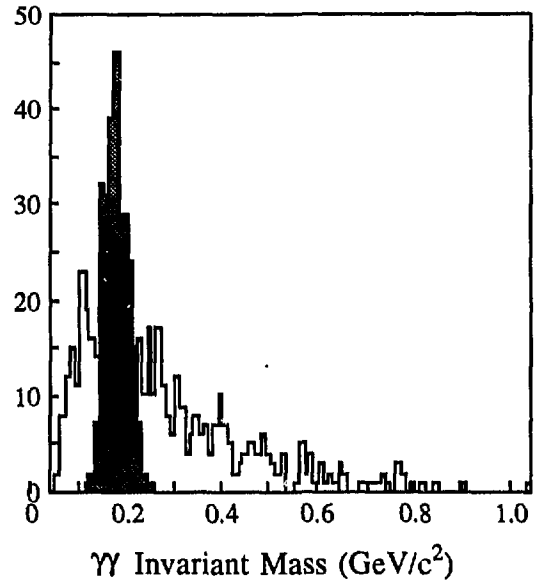

Figure 7.1: γ-γ Invariant Mass

meson decay if this energy sum is greater than 1 GeV. In order to be reasonably certain that the neutral energy is due to photons from π^0 or η decay and not to charged particle interactions in the Hex, electromagnetic shower fluctuations, or pattern recognition fakes, only photons with $E_\gamma \geq 0.4$ GeV are included in the energy sum.

Some confusion is possible if there is more than one π^0 candidate in the same hemisphere, in particular, when significant neutral energy is observed in addition to one π^0 candidate but not in addition to the other candidate. An event weighting scheme is used to resolve this ambiguity. The additional neutral energy sum is computed for each π^0 candidate in the hemisphere and the weight assigned to the decay is the fraction of π^0 candidates that have more than 1 GeV additional energy. Using this technique, a total of 47.5 multiple neutral meson decays are found in the 1299 τ_{1+1} events.

7.1.4 Background

In order to estimate the background contamination in the multiple neutral meson signal, $\tau^+\tau^-$ events are simulated with the Monte Carlo program described in Section 4.3. This program includes QED corrections from initial and final state radiation [34], a detailed detector section that simulates electromagnetic [32] and hadronic [36] showers in the Hex, and simulates $\tau^\pm$ decay with the branching fractions listed in Table 6.2. These showers are processed with the same photon reconstruction software (Section 4.1.3) and event selection software

(Section 5.2.1) as the real data. The Monte Carlo estimates that 7.6 ± 0.8 of the events in the multiple neutral meson sample are background events, mostly due to $\tau^- \to \nu_\tau \rho^- \to \nu_\tau \pi^- \pi^0$ decays accompanied by QED radiation.

7.2 Branching Fraction Measurement

This section describes how the number of multiple neutral meson decays identified in Section 7.1.3 is converted to the inclusive branching fraction for the decays $\tau^- \to \nu_\tau \pi^- \pi^0 + \mathrm{n}h^0$ ($\mathrm{n} \geq 1$), where h^0 is a π^0 or an η. The computation is complicated because three decay modes ($\tau^- \to \nu_\tau \pi^- \pi^0 \pi^0$, $\tau^- \to \nu_\tau \pi^- \pi^0 \pi^0 \pi^0$, and $\tau^- \to \nu_\tau \pi^- \pi^0 \eta$) are expected to contribute to the multiple neutral meson signal and the acceptance for each decay mode is different. In other words, the number of reconstructed multiple neutral meson decays (N_{MNM}) is proportional to a weighted sum of the three branching fractions,

$$N_{\mathrm{MNM}}(\text{reconstructed}) \propto w_1 \cdot B_{\nu_\tau \pi^- \pi^0 \pi^0} + w_2 \cdot B_{\nu_\tau \pi^- \pi^0 \pi^0 \pi^0} + w_3 \cdot B_{\nu_\tau \pi^- \pi^0 \eta}, \tag{7.1}$$

where the weights reflect the difference in acceptance for each decay mode. Therefore, the number of reconstructed decays is first converted into a weighted sum of the three branching fractions, then a photon counting argument is then used to limit the contribution from the $\tau^- \to \nu_\tau \pi^- \pi^0 \pi^0 \pi^0$ and $\tau^- \to \nu_\tau \pi^- \pi^0 \eta$ decay modes, which enables the weighted sum to be converted into an unweighted sum of the three branching fractions.

7.2.1 Measurement Method

The branching fraction is computed using the method described in Section 6.2.1, that is, the number of multiple neutral meson decays is compared to the number of τ_{1+1} events. The 47.5 multiple neutral decays are converted into branching fractions by solving Equations 7.2 and 7.3, which were derived in Section 6.2.1.

$$N_{\tau_{1+1}} = \sum_{exp} N_{\tau\tau}(exp) \cdot \sum_x \sum_y B_x \cdot B_y \cdot \epsilon_{trig}(exp, x, y) \cdot \epsilon_{select}(x, y), \tag{7.2}$$

$$\begin{aligned} N_{\mathrm{MNM}}(\text{reconstructed}) \;=\; & \\ & 2 \cdot \sum_{exp} N_{\tau\tau}(exp) \cdot \sum_{x \neq \mathrm{MNM}} B_x \cdot B_{\mathrm{MNM}} \cdot \\ & \quad \epsilon_{trig}(exp, x, \mathrm{MNM}) \cdot \epsilon_{select}(x, \mathrm{MNM}) \cdot \epsilon^1_{recon}(exp) \\ & + \sum_{exp} N_{\tau\tau}(exp) \cdot B_{\mathrm{MNM}} \cdot B_{\mathrm{MNM}} \cdot \epsilon_{trig}(exp, \mathrm{MNM}, \mathrm{MNM}) \cdot \\ & \quad \epsilon_{select}(\mathrm{MNM}, \mathrm{MNM}) \cdot [\epsilon^2_{recon}(exp) - 2\epsilon^1_{recon}(exp)] \end{aligned} \tag{7.3}$$

As before, $N_{\tau\tau}$ ($= \mathcal{L}_{e^+e^-} \cdot \sigma_{\tau^+\tau^-}$) is the total number of $\tau^+\tau^-$ events produced, ϵ_{trig} is the trigger efficiency, ϵ_{select} is the $\tau_{1\times1}$ event selection efficiency, $B_{\rm MNM}$ is the multiple neutral meson branching fraction, ϵ^n_{recon} is the average number of multiple neutral meson decays reconstructed if n multiple neutral meson decays are produced in an event (the allowed range for ϵ^n_{recon} is from 0 to n), and x and y are the possible $\tau^\pm$ one prong decay modes ($\sum_x B_x = B_1$). Again, all variables in Equations 7.2 and 7.3, with the exception of $N_{\tau\tau}$ and $B_{\rm MNM}$, can either be measured with the beam data or predicted by the Monte Carlo, so these two equations can be solved simultaneously to obtain a measurement for $B_{\rm MNM}$. Note that the values of ϵ_{trig}, ϵ_{select}, and ϵ^n_{recon} depend on the assumption for the multiple neutral meson decay mode, so Equations 7.2 and 7.3 are valid only for a single decay mode assumption.

7.2.2 Computation Details

The values for the variables in Equations 7.2 and 7.3 are obtained using the methods described in Section 6.2.2. The data are divided into three experimental periods corresponding to the different trigger configurations (Section 5.2.3) and the number of functional Hex modules (Section 3.3.5), summarized in Table 6.1. The values for the selection efficiencies $\epsilon_{select}(x,y)$ are listed in Table 5.1. These values are predicted with the Monte Carlo simulation as described in Section 5.2.1 and are between 15% and 25%, except for $\epsilon_{select}(e^+,e^-)$ which is $< 1\%$. Similarly, values for the trigger efficiencies $\epsilon_{trig}(exp,x,y)$ are listed in Table 5.2. These efficiencies are measured with beam data as described in Section 5.2.3 and are typically between 95% and 100%. The values for B_x listed in Table 6.2 are based on the Particle Data Book [5] values, but are adjusted slightly to sum to 100%.

Separate values for the reconstruction efficiencies $\epsilon^n_{recon}(exp)$ are determined by Monte Carlo simulation for each candidate multiple neutral meson decay mode. First, $\tau^+\tau^-$ events are generated with each $\tau^\pm$ decaying either to $\tau^- \rightarrow \nu_\tau\bar{\nu}_\mu\mu^-$ or to $\tau^- \rightarrow \nu_\tau\pi^-\pi^0\pi^0$. The number of identified multiple neutral meson decays is counted using the method described in Section 7.1.3, then divided by the number of generated multiple neutral meson decays to obtain a crude measurement of the reconstruction efficiency for the decay mode $\tau^- \rightarrow \nu_\tau\pi^-\pi^0\pi^0$. This crude measurement is corrected for the effect of inactive modules and repeated for the other two assumptions for the multiple neutral decay modes, $\tau^- \rightarrow \nu_\tau\pi^-\pi^0\pi^0\pi^0$ and $\tau^- \rightarrow \nu_\tau\pi^-\pi^0\eta$, to obtain the values for $\epsilon^n_{recon}(exp)$ listed in Table 7.2.

Equations 7.2 and 7.3 are solved for each of the three possible assumptions for the multiple neutral meson decay mode. That is, all multiple neutral meson decays are first assumed to be due to $\tau^- \rightarrow \nu_\tau\pi^-\pi^0\pi^0$ decays and $B_{\rm MNM}$ is calculated with this assumption. Next, the assumption for the decay mode is changed and $B_{\rm MNM}$ is calculated assuming all multiple neutral meson decays are due to $\tau^- \rightarrow \nu_\tau\pi^-\pi^0\pi^0\pi^0$ decays and $\tau^- \rightarrow \nu_\tau\pi^-\pi^0\eta$ decays, with the results listed in Table 7.3. The weights and proportionality constant that appear in the equation for the weighted sum of branching fractions (Equation 7.1) are

Decay Mode	Reconstruction Efficiency	5 Active Modules	4 Active Modules
$\tau^- \rightarrow \nu_\tau \pi^- \pi^0 \pi^0$	ϵ^1_{recon}	11.3%	9.2%
	ϵ^2_{recon}	20.9%	16.4%
$\tau^- \rightarrow \nu_\tau \pi^- \pi^0 \pi^0 \pi^0$	ϵ^1_{recon}	18.4%	14.6%
	ϵ^2_{recon}	37.5%	29.9%
$\tau^- \rightarrow \nu_\tau \pi^- \pi^0 \eta$	ϵ^1_{recon}	14.6%	11.2%
	ϵ^2_{recon}	31.0%	23.8%

Table 7.2: Multiple Neutral Meson Reconstruction Efficiency

Decay Mode Assumption	B_{MNM}
$\tau^- \rightarrow \nu_\tau \pi^- \pi^0 \pi^0$	13.9%
$\tau^- \rightarrow \nu_\tau \pi^- \pi^0 \pi^0 \pi^0$	8.8%
$\tau^- \rightarrow \nu_\tau \pi^- \pi^0 \eta$	12.9%

Table 7.3: Multiple Neutral Meson Branching Ratios

calculated by normalizing these values of B_{MNM} to the value of B_{MNM} obtained for the decay mode assumption $\tau^- \rightarrow \nu_\tau \pi^- \pi^0 \pi^0$, as this decay mode is expected to dominate. Therefore $w_1 = 1.0$, $w_2 = 13.9/8.8 = 1.6$, and $w_3 = 13.9/12.9 = 1.1$, and Equation 7.1 becomes

$$B_{\nu_\tau \pi^- \pi^0 \pi^0} + 1.6 \cdot B_{\nu_\tau \pi^- \pi^0 \pi^0 \pi^0} + 1.1 \cdot B_{\nu_\tau \pi^- \pi^0 \eta} = (13.9 \pm 2.0)\%, \qquad (7.4)$$

where the quoted error includes only the statistical error.

7.2.3 Systematic Errors

The two main contributions to the systematic error are the uncertainty in the π^0 reconstruction efficiency and the uncertainty in the background subtraction. Fortunately, it is possible to measure the magnitude both of these systematic errors.

The error due to the π^0 reconstruction efficiency is found by measuring the branching fraction $\tau^- \rightarrow \nu_\tau \rho^-$, as errors in the π^0 reconstruction efficiency are directly reflected in the measurement of the branching fraction. In Section 6.2.4, the branching fraction for $\tau^- \rightarrow \nu_\tau \rho^-$ decays is measured to be (22.6±3.1)% (statistical error only), which agrees with the world average of (22.1 ± 1.4)% [5,37]. The branching fraction is nearly linearly proportional to the π^0 reconstruction efficiency, so an upper limit on the systematic error due to π^0 reconstruction efficiency is given by the statistical error in the branching fraction measurement

Error Source	Error (%)
π^0 Reconstruction Eff.	13.7
Background Subtraction	5.0
B_π	3.6
ϵ_{trig}	2.2
ϵ_{select}	2.2
Luminosity	1.1
B_1	0.7
Total	15.4

Table 7.4: Systematic Errors

divided by the measurement, or $3.1/22.6 = 13.7\%$. A similar check of the π^0 reconstruction efficiency is made by comparing the inclusive π^0 cross section to the inclusive $\pi^\pm$ cross section in multi-hadron events. The ratio $2\sigma_{\pi^0}/(\sigma_{\pi^+} + \sigma_{\pi^-})$, which should be unity, is measured to be (0.92 ± 0.14) [40], so this measurement limits the systematic error due to the uncertainty in the π^0 reconstruction efficiency to 14%.

The systematic error due to background subtraction is checked using three charged prong $\tau^\pm$ decays. Of the τ^- decays that involve three charged particles, approximately 60% are $\tau^- \to \nu_\tau \pi^- \pi^+ \pi^-$, approximately 40% are $\tau^- \to \nu_\tau \pi^- \pi^+ \pi^- \pi^0$, and less than 0.5% are due to decays with more than one neutral meson [2,21]. When the three charged track decays in the 660 events in the τ_{1+3} sample (Section 5.3) are searched for multiple neutral meson decays using the same method that is used for single prong $\tau^\pm$ decays (Section 7.1.3), 10.0 ± 3.2 (statistical error) events are found, while the Monte Carlo predicts 9.2 events. Since the Monte Carlo and the data agree, an upper limit on the error in the background rate is $3.2/10.0 = 32\%$, which leads to a systematic error due to uncertainty in background subtraction of 5.0%.

The contributions to the systematic error from all other sources are small compared to the error due to the uncertainty in the π^0 reconstruction efficiency and the background subtraction. Their contributions are estimated by changing each variable by 10% to 20% of its nominal value, then re-calculating the weighted branching fraction. Table 7.4 lists all contributions to the systematic error quoted as a percentage of the branching fraction, which are added in quadrature to obtain the total systematic error. Therefore, Equation 7.4 becomes

$$B_{\nu_\tau \pi^- \pi^0 \pi^0} + 1.6 \cdot B_{\nu_\tau \pi^- \pi^0 \pi^0 \pi^0} + 1.1 \cdot B_{\nu_\tau \pi^- \pi^0 \eta} = (13.9 \pm 2.0 \pm 2.1)\%, \qquad (7.5)$$

where the first error is the statistical error and the second error is the systematic error.

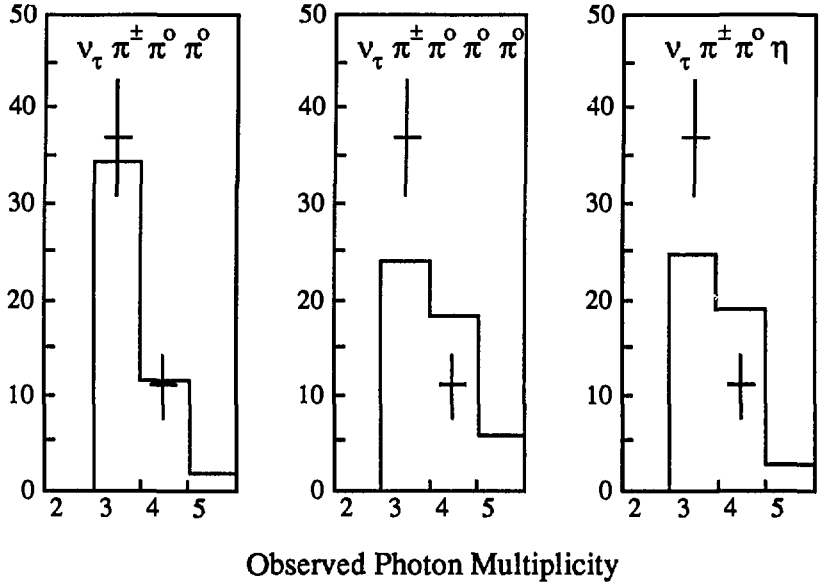

Figure 7.2: Observed Photon Multiplicity

7.2.4 Photon Counting

The contribution to the weighted sum of branching fractions (Equation 7.5) from $B_{\nu_\tau\pi^-\pi^0\pi^0\pi^0}$ and $B_{\nu_\tau\pi^-\pi^0\eta}$ is limited by counting the number of photons observed in multiple neutral meson decays. The Monte Carlo predicts a significantly smaller [illegible] of detected photons for $\tau^- \to \nu_\tau\pi^-\pi^0\pi^0$ decays than for $\tau^- \to \nu_\tau\pi^-\pi^0\pi^0\pi^0$ or $\tau^- \to \nu_\tau\pi^-\pi^0\eta$ decays (Figure 7.2). In this figure, the solid lines correspond to the Monte Carlo prediction and the points with error bars are from beam data. When the observed photon multiplicity is fit to a linear combination of the distributions predicted for each decay mode, the maximum likelihood is obtained if 100% of the multiple neutral meson signal is attributed to $\tau^- \to \nu_\tau\pi^-\pi^0\pi^0$ decays. However, the statistical error is large, so this result is expressed as a lower limit of

$$B_{\nu_\tau\pi^-\pi^0\pi^0} > 8.3\% \text{ (95\% CL)}, \tag{7.6}$$

or equivalently as an upper limit on the weighted sum of the remaining branching fractions of

$$1.6 \cdot B_{\nu_\tau\pi^-\pi^0\pi^0\pi^0} + 1.1 \cdot B_{\nu_\tau\pi^-\pi^0\eta} < 5.6\% \text{ (95\% CL)}. \tag{7.7}$$

7.2.5 Final Result

The final task is to convert the weighted sum of the multiple neutral meson branching fractions (Equation 7.5) into an unweighted sum of branching fraction. In order to perform this conversion, it is necessary to know the relative

contribution from each of the three candidate decay modes. This information is provided by Equation 7.7, the upper limit on the weighted sum of $B_{\nu_\tau\pi^-\pi^0\pi^0\pi^0}$ and $B_{\nu_\tau\pi^-\pi^0\eta}$. Since all candidate decay modes have a similar weight and the contribution of all but one mode is limited, the weighted sum is converted to an unweighted sum by modestly increasing the systematic error.

Since the best fit is obtained when $B_{\nu_\tau\pi^-\pi^0\pi^0\pi^0}$ and $B_{\nu_\tau\pi^-\pi^0\eta}$ are 0% (Equation 7.7), the most probable value for the unweighted sum is 13.9%. Therefore, we measure an unweighted sum of the multiple neutral meson branching fractions of

$$B_{\nu_\tau\pi^-\pi^0\pi^0} + B_{\nu_\tau\pi^-\pi^0\pi^0\pi^0} + B_{\nu_\tau\pi^-\pi^0\eta} = (13.9 \pm 2.0^{+2.1}_{-2.4})\%, \qquad (7.8)$$

where the uncertainty in the composition of the multiple neutral meson decay modes is now included in the systematic error. The systematic errors in Equation 7.8 are asymmetric, as non-zero values for $B_{\nu_\tau\pi^-\pi^0\pi^0\pi^0}$ and $B_{\nu_\tau\pi^-\pi^0\eta}$ can lower the unweighted sum but not raise it. The values for the additional systematic error are given by the extreme values for the unweighted sum obtained when the three multiple neutral meson branching fractions are independently varied within the one standard deviation contour defined by Equations 7.5 and 7.7.

Since it is assumed that only these three decay modes contribute to the multiple neutral meson branching fraction, Equation 7.8 is equivalently written as

$$B(\tau^- \to \nu_\tau\pi^-\pi^0 + \mathrm{n}h^0) = (13.9 \pm 2.0^{+2.1}_{-2.4})\%, \qquad (7.9)$$

where h^0 is a π^0 or an η and $\mathrm{n} \geq 1$.

Chapter 8

Summary and Conclusions

This dissertation presents a measurement for the inclusive multiple neutral meson branching fraction of the tau lepton of

$$B(\tau^- \to \nu_\tau \pi^- \pi^0 + \mathrm{n}h^0) = (13.9 \pm 2.0^{+2.1}_{-2.4})\%, \tag{8.1}$$

where h^0 is a π^0 or an η and $\mathrm{n} \geq 1$. This result is more than four standard deviations from zero, and so more significant than the only previous measurement [6] of

$$B(\tau^- \to \nu_\tau \pi^- \pi^0 \pi^0) + B(\tau^- \to \nu_\tau \pi^- \pi^0 \pi^0 \pi^0) = (9.0 \pm 4.4)\%. \tag{8.2}$$

The measurement presented here resolves the $(17.6 \pm 2.0)\%$ discrepancy between the inclusive and sum of the exclusive one prong branching fractions. When this measurement is included in the sum of measured exclusive one prong branching fractions of the τ^-, the difference between the inclusive and sum of exclusive branching fractions becomes $(3.7^{+3.7}_{-3.5})\%$. The discrepancy is now consistent with zero, although this is partly due to the increased error in the sum of exclusive branching fractions.

This experiment has some power to distinguish between multiple neutral meson decay modes, and so measures a lower limit of

$$B(\tau^- \to \nu_\tau \pi^- \pi^0 \pi^0) > 8.3\% \text{ (95\% CL)}, \tag{8.3}$$

or equivalently, an upper limit of

$$1.1 \cdot B(\nu_\tau \pi^- \pi^0 \eta) + 1.6 \cdot B(\nu_\tau \pi^- \pi^0 \pi^0 \pi^0) < 5.6\% \text{ (95\% CL)}. \tag{8.4}$$

This measurement confirms the theoretical prediction that the inclusive multiple neutral meson branching fraction is dominated by $B(\tau^- \to \nu_\tau \pi^- \pi^0 \pi^0)$, but indicates that the theoretical prediction of 7.1% for $B(\tau^- \to \nu_\tau \pi^- \pi^0 \pi^0)$ is slightly low.

It is possible that this disagreement is explained by errors in the prediction for $B(\tau^- \to \nu_\tau \pi^- \pi^0 \pi^0)$. This prediction is based on isospin arguments and the measured value of $B(\tau^- \to \nu_\tau \pi^- \pi^+ \pi^-)$, and while the isospin arguments are likely to be correct, the measurement of $B(\tau^- \to \nu_\tau \pi^- \pi^+ \pi^-)$ has an error of

approximately 0.8%. In addition, Table 2.5 shows that there is an anomalously low measurement of $B(\tau^- \to \nu_\tau \pi^- \pi^+ \pi^-)$ that pulls the weighted average down. If this measurement is ignored, the weighted average climbs to $(7.7 \pm 0.6)\%$ and the difference between the theoretical prediction and the measurement of $B(\tau^- \to \nu_\tau \pi^- \pi^0 \pi^0)$ is reduced to about two standard deviations.

Unfortunately, the measurements presented here are not sensitive enough to determine why the theoretical prediction for the discrepancy is incorrect. However, it is possible to present a scenario that resolves the discrepancy and still agrees (within two standard deviations) with all current measurements and solid theoretical predictions. If the true value of $B(\tau^- \to \nu_\tau \pi^- \pi^+ \pi^-)$ is 8.5%, which is less than two standard deviations from its current value, the predicted sum of exclusive multiple neutral meson branching fractions would increase from 9.4% to 10.8% and the predicted value of $B(\tau^- \to \nu_\tau \pi^- \pi^0 \pi^0)$ would be consistent with the results in Equation 8.3. In addition, the theoretical prediction for $B(\tau^- \to \nu_\tau \pi^- \pi^0 \eta)$ is not very sound (Section 2.3), so the true value of this branching fraction could be as high as 5.0% without presenting any theoretical difficulties. If the true value of $B(\tau^- \to \nu_\tau \pi^- \pi^0 \eta)$ is 5.0%, which is consistent with Equation 8.4, then the sum of exclusive multiple neutral meson branching fractions would be 15.8%, which is consistent with the current value of the discrepancy of $(17.6 \pm 2.0)\%$.

This dissertation has shown that the discrepancy between the inclusive and sum of the exclusive single prong branching fractions of the τ^- is due to decay modes that involve more than one neutral meson. However, more work is necessary to understand completely the decay modes of the τ^-. In particular, high precision measurements of the individual branching fractions for multiple neutral meson decay modes are necessary to truly the theoretical predictions conclusively. A precise measurement of $B(\tau^- \to \nu_\tau \pi^- \pi^0 \eta)$ would be especially interesting, as the theoretical predictions for this branching fraction are not very reliable.

Bibliography

[1] F.J. Gilman and S.H. Rhie. *Phys. Rev. D* **31**, 1066 (1985).

[2] E. Fernandez, et al. *Phys. Rev. Lett.* **54**, 1624 (1985).

[3] C. Akerlof, et al. *Phys. Rev. Lett.* **55**, 570 (1985).

[4] I. Beltrami, et al. *Phys. Rev. Lett.* **54**, 1775 (1985).

[5] M. Aguilar-Benitez, et al. Review of particle properties. *Phys. Lett.* **170B**, 1 (1986).

[6] H.J. Behrend, et al. *Z. Phys. C* **23**, 103 (1984). The experimental method used to measure these branching fractions is based almost entirely on photon counting arguments, which gives large correlations between the measurements of $B(\tau^- \to \nu_\tau \pi^- \pi^0)$, $B(\tau^- \to \nu_\tau \pi^- \pi^0 \pi^0)$, and $B(\tau^- \to \nu_\tau \pi^- \pi^0 \pi^0 \pi^0)$. In addition, analyses based on photon counting tend to be very sensitive to the Monte Carlo simulation of the photon reconstruction efficiency. However, the results of this analysis are presented with relatively small total systematic errors (1.8%) and without any significant discussion of either the correlations among branching fractions or the systematic errors. The significance of the quoted branching fractions is small, and if the systematic errors are arbitrarily doubled in hopes of simulating a more reasonable error, the significance of the results nearly vanishes. Therefore, this dissertation treats the branching fractions for these decay modes as if they have not yet been measured.

[7] S.L. Glashow. *Nucl. Phys.* **22**, 579 (1961).

[8] S. Weinberg. *Phys. Rev. Lett.* **19**, 1264 (1967).

[9] A. Salam. In N. Svartholm, editor, *Proceedings of the Eighth Nobel Symposium*, page 367, Wiley Interscience, New York, 1968.

[10] M.L. Perl, et al. *Phys. Rev. Lett.* **35**, 1489 (1975).

[11] W. Bacino, et al. *Phys. Rev. Lett.* **41**, 13 (1978).

[12] M.L. Perl. *Ann. Rev. Nucl. Part. Sci.* **30**, 299 (1980).

[13] J. Kirkby. In T. Kirk and H. Abarbanel, editors, *Proceedings of the 1979 International Symposium on Lepton and Photon Interactions at High Energies*, page 107, Batavia, IL, 1979.

[14] W. Bartel, et al. *Phys. Lett.* **161B**, 188 (1985).

[15] S. Behrends, et al. *Phys. Rev. D* **32**, 2468 (1985).

[16] K.G. Hayes, et al. *Phys. Rev. D* **25**, 2869 (1982).

[17] G.E. Forden. In E. Brennan, editor, *Proceedings of the Thirteenth SLAC Summer Institute in Particle Physics*, page 497, Stanford, CA, 1985.

[18] E.D. Commins. *Weak Interactions.* McGraw-Hill, New York, 1973.

[19] Y.S. Tsai. *Phys. Rev. D* **4**, 2821 (1971).

[20] W. Ruckstuhl, et al. *Phys. Rev. Lett.* **56**, 2132 (1986).

[21] W.B. Schmidke, et al. *Phys. Rev. Lett.* **57**, 527 (1986).

[22] M. Peshkin and J.L. Rosner. *Nucl. Phys.* **B122**, 144 (1977).

[23] G.B. Mills, et al. *Phys. Rev. Lett.* **54**, 624 (1985).

[24] Patricia R. Burchat. *Decay of the Tau Lepton.* PhD thesis, Stanford University, February 1986. SLAC-292.

[25] C. Matteuzzi, et al. *Phys. Rev. D* **32**, 800 (1985).

[26] H. Aihara, et al. *IEEE Trans. Nucl. Sci.* **NS30**, 153 (1983).

[27] R. Fuzesy, N.J. Hadley, and P.R. Robrish. *Nucl. Instr. Meth.* **233**, 40 (1984).

[28] H. Aihara, et al. *Nucl. Instr. Meth.* **217**, 259 (1983).

[29] H. Aihara, et al. *IEEE Trans. Nucl. Sci.* **NS30**, 67 (1983).

[30] M. Michaels, private communication. I would like to thank Dr. Michaels for the detective work that he did to understand the chemical reactions that disabled the Hex. Without his effort, the damage (as well as our understanding of the problem) would have been significantly worse.

[31] J. William Gary. *Tests of Models for Parton Fragmentation in e^+e^- Annihilation.* PhD thesis, University of California, Berkeley, November 1985. LBL-20638.

[32] R.L. Ford and W.R. Nelson. *The EGS Code System: Computer Programs for the Monte Carlo Simulation of Electromagnetic Cascade Showers (Version 3).* SLAC Report SLAC-210, Stanford Linear Accelerator Center, 1978.

[33] Marjory D. Shapiro. *Inclusive Hadron Production and Two Particle Correlations in e^+e^- Annihilation at 29 GeV Center-of-Mass Energy.* PhD thesis, University of California, Berkeley, December 1984. LBL-18820.

[34] F.A. Berends, et al. *Nucl. Phys.* **B202**, 63 (1982).

[35] T. Sjöstrand. *Comput. Phys. Commun.* **27**, 243 (1982).

[36] A. Grant. *Nucl. Instr. Meth.* **131**, 167 (1975).

[37] J.M. Yelton, et al. *Phys. Rev. Lett.* **56**, 812 (1986).

[38] J.D. Jackson. *Nuovo Cimento* **34**, 1644 (1964).

[39] G. Kalbfleisch. *Some Multiparticle Distributions of Massless Particles from the Lorentz Invariant Phase Space.* Group A Physics Note 157, Lawrence Berkeley Laboratory, 1960.

[40] H. Aihara, et al. *Z. Phys. C* **27**, 187 (1985).